Robotica (2026), **44**, pp. 1325–1355
doi:10.1017/S0263574726103464

CAMBRIDGE UNIVERSITY PRESS

RESEARCH ARTICLE

Wobble control of a pendulum-based spherical robot

Vidyut Balaji[1], Animesh Singhal[2], Sahil Modi[1], Abhishek Gupta[1] and Leena Vachhani[2]

[1]Department of Mechanical Engineering, Indian Institute of Technology Bombay, India
[2]Centre for Systems and Control, Indian Institute of Technology Bombay, India
Corresponding author: Abhishek Gupta; Email: abhi.gupta@iitb.ac.in

Received: 3 June 2025 UTC; **Revised:** 2 April 2026 UTC; **Accepted:** 9 April 2026 UTC;
First published online: 24 June 2026 UTC

Keywords: Lagrange D'Alembert; non-holonomic constraints; wobbling; precession; spherical robot; radius of curvature; pendulum; Euler angles; robotics; Coulomb friction; mechanics; controller design; input–output feedback linearization; point-to-point navigation

Abstract

Spherical robots can conduct surveillance in hostile, cluttered environments without being damaged. Their protective shell can safely house sensors and sensitive components. The pendulum-based spherical robot provides a platform (yoke) for a camera to be housed inside the protective hull. However, lateral oscillations, also known as wobble, become prominent when operated at low speeds, leading to shaky camera feedback. These oscillations are caused by the coupling between the forward and steering motions due to nonholonomic constraints. Designing a controller to limit wobbling in these robots is challenging due to their underactuated nature. In this paper, we propose a model-based (wobble-free) controller to navigate a pendulum-steered spherical robot to perform wobble-free turning maneuvers consisting of circular arcs and straight lines. The model is developed using Lagrange-D'Alembert equations and accounts for the coupled forward and steering motions. Furthermore, we also propose quantifiable metrics for wobble by deriving expressions for radius of curvature, precession rate, wobble amplitude, and wobble frequency during circular motions and designed an input–output feedback linearization-based controller to control the robot's heading direction and wobble. Additionally, we extend the controller's capabilities to handle point-to-point navigation, enabling the robot to execute more complex and goal-oriented trajectories. This research ensures the robot maintains wobble-free motion across diverse paths, enhancing its navigational autonomy and the quality of camera feedback. Overall, the proposed controller enables a teleoperator to command a specific forward velocity and pendulum angle as per the desired turning radius or destination while effectively limiting the robot's lateral oscillations.

Nomenclature

T_s	Rolling torque on the hull with respect to the yoke, results in forward rolling motion of the robot
T_p	Pendulum torque on the pendulum with respect to the yoke, results in lateral motion of the robot
r_p	Distance between the pendulum's center of mass and hull's geometric center
r_h	Radius of the hull (spherical shell)
r_y	Distance between the yoke's center of mass and hull's geometric center
G	Global inertial frame fixed to the ground
Y	Frame attached to the yoke
P	Frame attached to the pendulum
H	Frame attached to the hull

© The Author(s), 2026. Published by Cambridge University Press.

https://doi.org/10.1017/S0263574726103464 Published online by Cambridge University Press

ϕ	Heading angle of the robot measured with respect to the X-axis of global frame **G**. This angle characterizes the precession of the robot.
θ	Lean angle of the robot perpendicular to the heading direction. This angle characterizes the lateral oscillations or **wobbling** of the robot
ψ	Forward spin angle of the robot responsible for moving it forward or backwards. This angle characterizes the forward rolling of the robot.
β	Pendulum angle relative to the yoke
${}^{\mathbf{A}}\mathbf{R}_{\mathbf{B}}$	Rotation matrix of frame **A** with respect to frame **B**
${}^{\mathbf{A}}\vec{\omega}_{\mathbf{A}}$	The angular velocity vector of frame **A** expressed in frame **A**
${}^{\mathbf{A}}_{\mathbf{B}}\vec{r}_{\mathbf{P}}$	Position vector of a point **P** starting from the origin of coordinate frame **B** expressed in frame **A**
$\mathbf{Y}_c$	Position vector corresponding to the center of mass of yoke
$\mathbf{H}_c$	Position vector corresponding to the center of mass of hull
$\mathbf{P}_c$	Position vector corresponding to the pendulum's center of mass
$\mathbf{P}_o$	Position vector corresponding to the origin of pendulum frame
X, Z	X and Z co-ordinates of the hull center along the global frame **G**($OXYZ$)
${}^{\mathbf{A}}\vec{v}_{\mathbf{P}}$	Linear velocity vector of point **P** expressed in frame **A**
K	Kinetic energy of the system
V	Potential energy of the system
m_B	mass of a body B
${}^{\mathbf{B}}I_{\mathbf{B}}$	The mass moment of inertia matrix of a body B calculated in its own frame of reference
λ_i	Lagrange multipliers
L	Lagrangian
$\mathbf{x}$	State vector representing robot's motion
u	Control input
q	Generalized coordinates
Q	Generalized forces
A	Amplitude of lateral oscillations
ω	Frequency of lateral oscillations
ρ	Radius of curvature for a spherical robot moving in a circular trajectory with pure rolling
y	Control output
$K_{p,\dot{\psi}}$	Speed control gain
$K_{p,\beta}$	Proportional component of pendulum control gain
$K_{d,\beta}$	Derivative component of pendulum control gain
$K_{p,\dot{\theta}}$	Wobble control gain
$T_{p,\dot{\theta}}$	Wobble control component of pendulum torque
$T_{p,\beta}$	Pendulum control component of pendulum torque
$\dot{\theta}_{des}$	Desired value of the rate of change of lean angle
$\dot{\psi}_{des}$	Desired value of forward speed
β_{des}	Desired value of the pendulum's angle
γ, δ	Coefficients of a linear combination

1. Introduction

Spherical robots offer a distinct advantage by enclosing all electro-mechanical components within a protective shell, shielding them from harsh environments and external impacts. Their ball-shaped design gives them the ability to recover effortlessly from collisions, preventing entrapment in corners. Furthermore, recent advancements highlight pendulum-based designs as they possess inherent stability thanks to their shape [1], enabling them to regain equilibrium after disturbances. This characteristic proves invaluable in scenarios where they are thrown or fall from heights. These advantages make them

https://doi.org/10.1017/S0263574726103464 Published online by Cambridge University Press

ideal for a wide range of applications, including surveillance, reconnaissance, hazardous environment assessment, search and rescue, and planetary exploration [2–4]. Spherical robots also find purpose as therapeutic and educational tools for children with developmental disorders, implying usefulness outside terrestrial exploration [5].

Despite these advantages, experimental studies have consistently reported the presence of lateral oscillations, commonly referred to as wobble, in pendulum-driven spherical robots operating at various pendulum angles [6–8]. Early work by Froberg and Smolic [9] identified this wobbling behavior and proposed a PID-based approach to mitigate tipping errors induced by pendulum motion. Similarly, Schroll [10] developed a detailed model of a spherical robot actuated by a two-degree-of-freedom pendulum, demonstrating that steering via a fixed pendulum inclination leads to wobbly circular trajectories characterized by lateral oscillations and a time-varying radius of curvature. Although these oscillations are usually small in magnitude and therefore overlooked, they become critical in applications involving onboard cameras or sensors, where even minor deviations can degrade data quality. Consequently, suppressing wobble is essential for achieving reliable perception and improved navigational autonomy. This, in addition to improvements in perception with panoramic camera setups for real-time object detection [11], makes spherical robots a very strong surveillance and exploration solution.

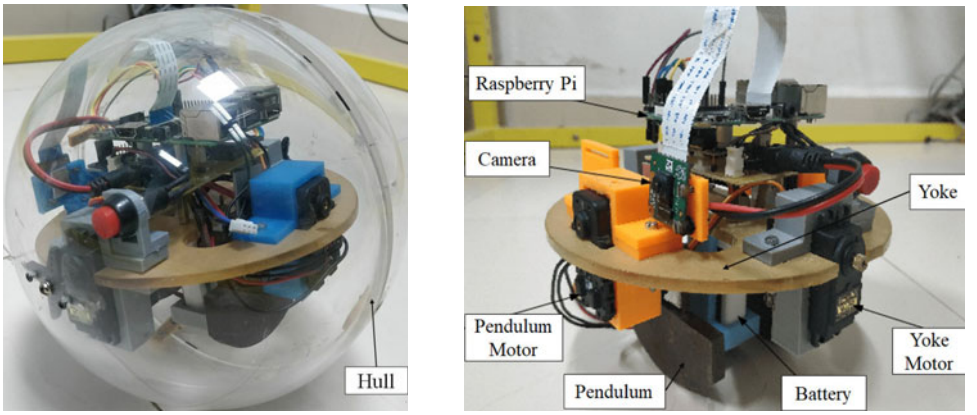
The control of spherical robots is inherently challenging due to their nonholonomic constraints, underactuated nature, and non-chained system structure [12–14]. These challenges become more pronounced in non-ideal environments such as inclined terrains, where maintaining stability and accurate motion control is significantly more difficult [15]. A variety of advanced control strategies have been proposed to address these challenges. For instance, recurrent neural network-based controllers have been developed to handle uncertainties and actuator saturation [16], while reinforcement learning approaches have recently been explored for autonomous navigation [17]. Classical control techniques, including Lyapunov-based methods combined with neurodynamic approaches, have also been employed for trajectory tracking [18]. In addition, adaptive high-speed sliding mode control strategies have been proposed to improve maneuverability under dynamic uncertainties [19]. Direction and trajectory tracking control schemes for nonholonomic spherical robots have also been investigated to enhance tracking accuracy under constrained motion dynamics [20]. Furthermore, Hogan and Forbes [21] proposed a control framework for regulating heading and forward velocity in pendulum-actuated spherical robots. However, none of these approaches address the suppression of lateral oscillations.

Some studies have attempted to mitigate wobbling behavior, albeit with limited success. One approach [22] selects control outputs to regulate speed while minimizing pendulum oscillations; however, residual wobble persists, and unrestricted pendulum motion is often impractical due to spatial constraints within the shell. Sliding mode control strategies [23] have also been explored to regulate forward speed and lean angle, but they suffer from issues such as chattering and sensitivity to parameter tuning. In the context of Ballast Mass Fixed Axis designs, some works have focused on regulating lean angle using decoupled models [24], which neglect the coupling between linear and steering dynamics and therefore fail to eliminate wobble in practice. Other approaches employ system identification techniques to account for external disturbances [25] but do not address oscillations arising from intrinsic system dynamics during turning maneuvers. These limitations highlight the need for a modeling and control framework that explicitly captures and addresses the coupled dynamics responsible for wobble.

The motion capabilities of spherical robots are strongly influenced by their actuation mechanisms [26, 27]. Existing designs can be broadly classified into direct driving methods [28], gravity-driven mechanisms (including pendulum-based systems [29–32] and gimbal-based configurations), angular momentum-driven systems utilizing flywheels [33], outer-shell deformation approaches [34], and hybrid mechanisms [35]. Recent work [36] has explored cylindrical pendulum configurations to improve spatial efficiency within the robot; these designs, however, do not explicitly address wobble observed at low speeds.

Corresponding to these diverse actuation strategies, a wide range of modeling approaches have been proposed to capture the complex dynamics of spherical robots. Early foundational work has established the nonholonomic nature and motion planning challenges of spherical robots through rigorous dynamic

https://doi.org/10.1017/S0263574726103464 Published online by Cambridge University Press



(a) Assembled robot (b) Components of the spherical robot

Figure 1. *The spherical robot.*

analysis [13]. First-order mathematical models based on rolling constraints and angular momentum conservation [46] provided initial insights into system behavior. More advanced formulations using Lagrangian methods and Euler angles have been widely adopted for modeling spherical motion on planar surfaces [37, 38]. In addition, alternative formulations such as the Boltzmann–Hamel framework have been employed to derive dynamic models that more effectively capture nonholonomic constraints and system coupling [39]. While some studies simplify the problem by decoupling forward and steering dynamics [40, 41] or by modeling circular motion through gyroscopic precession [42], others employ separate Euler–Lagrange formulations for different motion components [43–45]. However, these approaches often neglect the inherent coupling between lateral and longitudinal dynamics and consequently fail to capture the wobble observed in real systems. This gap motivates the need for a unified dynamic model that explicitly accounts for such coupling and enables systematic analysis and control of lateral oscillations.

This research focuses on a simulation-based analysis of a distinctive spherical robot with a yoke-pendulum design, illustrated in Figure 1. The yoke acts as a versatile platform for housing cameras, sensors, and electronic equipment. Two actuators drive the robot's motion: one rotates the shell, enabling forward and backward movement, while the other rotates the pendulum relative to the yoke. The latter shifts the robot's center of mass, hence steering the robot using gyroscopic effects. The pendulum's swinging motion is restricted to the lower hemisphere, as the upper hemisphere accommodates sensors and other components on the yoke. The driving mechanism employed by this spherical robot is commonly referred to as the Ballast–Mass Fixed Axis Design, combining elements of gravity and angular momentum driving methods found in the literature.

This work makes the following contributions, which are organized into separate sections:

Section 2: Kinematic model and dynamic analysis of wobble present in the motion of a spherical robot by developing equations that account for the coupling of its forward and steering motions. This underactuated system is modeled using Lagrange-D'Alembert equations that take the frames using Euler angles and non-holonomic constraints into account with Lagrange multipliers. We also modify the model for conditions of slipping.

Section 3: A simplified version of the model for circular motion and formulation for the wobble amplitude, wobble frequency, radius of curvature, and the precession rate associated with the robot's circular motion. The section concludes by comparing the system response generated by the actual model with that generated by the simplified model equations, demonstrating their similarity at different speeds.

https://doi.org/10.1017/S0263574726103464 Published online by Cambridge University Press

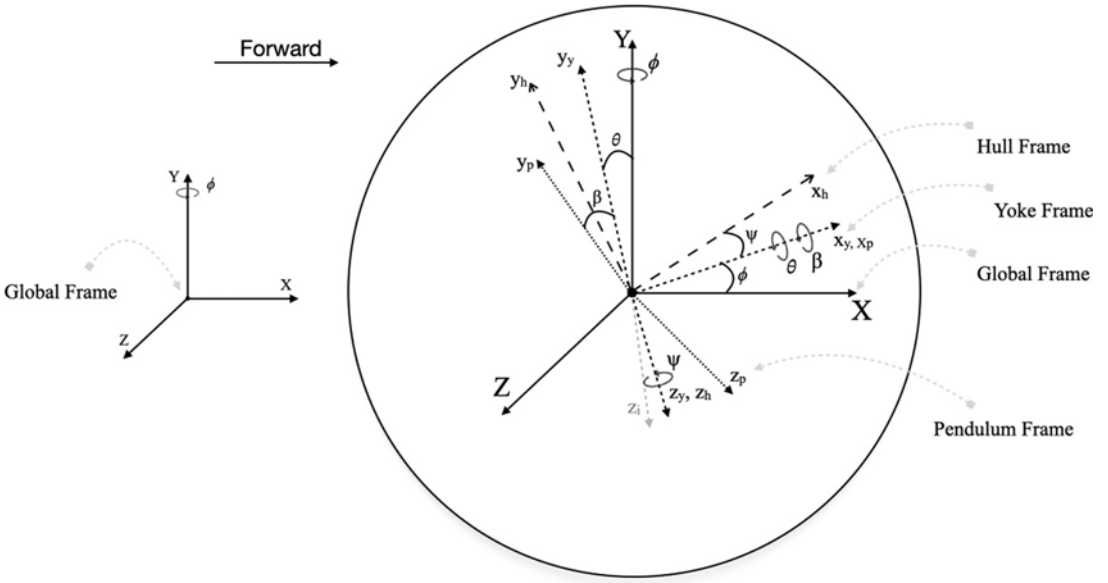


Figure 2. *Frames and Euler angles (YXZ)*

Section 4: We propose a feedback linearization-based controller design for controlling the spherical robot's heading direction via a turning maneuver while limiting its wobble and maintaining a stable and constrained pendulum motion.

Section 5: We demonstrate the versatility of the controller designed in the previous section, using a point-to-point navigation algorithm developed in our lab for both slip and no-slip conditions.

2. Modeling and dynamics

This section discusses the modeling of the pendulum-actuated spherical robot described in this work. The robot's pendulum is mounted on the yoke at the geometric center of the hull through a motor that provides a torque T_p. The yoke and the hull are connected through a motor mounted on the yoke. This motor rotates the hull by providing a torque T_s. The center of mass of the hull and the yoke are at the geometric center of the hull, while the pendulum's center of mass is at a distance r_p from the geometric center. Using the Lagrange D'Alembert formulation, we determine the equations of motion for this system under both pure rolling and slip conditions.

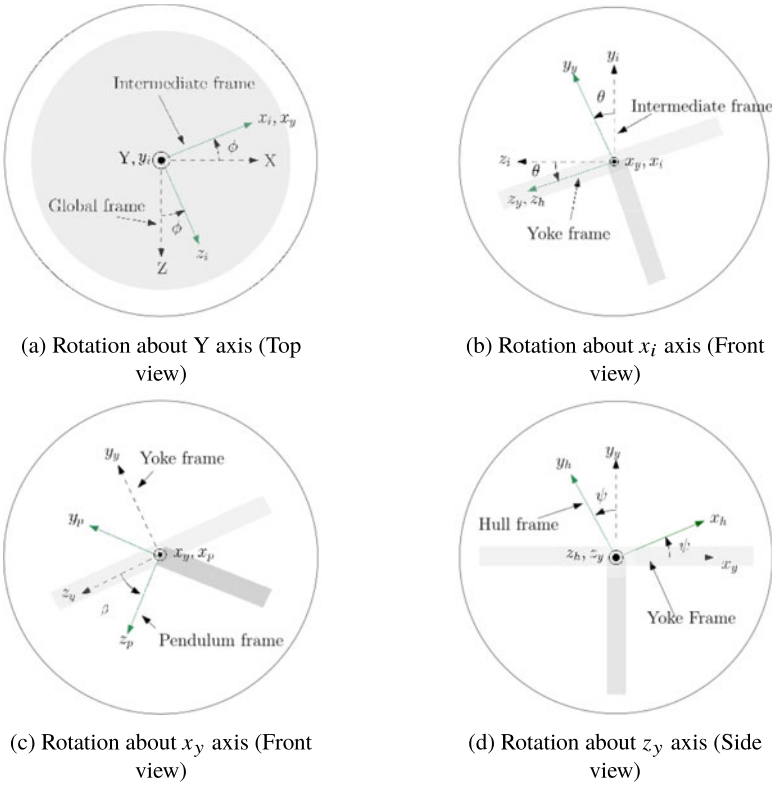
2.1. Reference frames and Euler Angles

This work is based on four reference frames, as shown in Figure 2: a global inertial frame fixed to the ground (**G**) and the three frames attached to the yoke (**Y**), pendulum (**P**), and hull (**H**), respectively, with their origins at the geometric center of the hull. The yoke frame **Y** is defined to meet the following constraints: (1) The z-axis of the yoke is always aligned with the z-axis of the hull, and (2) The x-axis of the yoke frame lies in the global XZ-plane, i.e., it always remains parallel to the ground.

The orientation of the hull at any given instant is characterized by three YXZ Euler angles ϕ, θ, and ψ. The orientation of the pendulum requires another angle β due to an additional degree of freedom. The transformation between frames happens as follows:

- Intermediate Frame (**I**): **G** is rotated along its Y-axis by angle ϕ to obtain **I** as shown in Figure 3a.
- Yoke frame (**Y**): **I** is rotated along its local x-axis x_i by angle θ to obtain **Y** as shown in Figure 3b.

https://doi.org/10.1017/S0263574726103464 Published online by Cambridge University Press



(a) Rotation about Y axis (Top view)

(b) Rotation about x_i axis (Front view)

(c) Rotation about x_y axis (Front view)

(d) Rotation about z_y axis (Side view)

Figure 3. *Steps for obtaining the frames.*

- Pendulum frame (**P**): **Y** is rotated along its local x-axis x_y by angle β to obtain **P** as shown in Figure 3c. Note that the angle made by the pendulum with the vertical axis Y is $(\beta + \theta)$.
- Hull frame (**H**): **Y** is rotated along its z-axis z_y by angle ψ to obtain **H** as shown in Figure 3d.

Careful design considerations are implemented in this system to avoid the gimbal lock problem. The yoke frame, obtained by rotating the intermediate frame along its local x-axis, never reaches a vertical orientation where gimbal lock occurs. This is crucial to maintain optimal functionality, as a complete 90-degree tilt of the robot would result in a horizontal camera, limiting the field of view. Preventive measures have also been taken by restricting the pendulum's angular displacement to the lower hemisphere of the robot and by housing all the electronics in the upper hemisphere. Furthermore, the control objectives and setpoints are meticulously chosen to minimize significant deviations from the mean lean angle, ensuring efficient operation of the system.

2.2. Robot kinematics

Rotation matrices mapping vectors from frames **Y**, **P**, and **H** to **G** are given by, ${}^{\mathbf{G}}\mathbf{R}_{\mathbf{Y}} = R_y(\phi)R_x(\theta)$, ${}^{\mathbf{G}}\mathbf{R}_{\mathbf{P}} = R_y(\phi)R_x(\theta)R_x(\beta)$, and ${}^{\mathbf{G}}\mathbf{R}_{\mathbf{H}} = R_y(\phi)R_x(\theta)R_z(\psi)$.
The angular velocities of different frames are obtained to be:

$$ {}^{\mathbf{Y}}\vec{\omega}_{\mathbf{Y}} = \begin{bmatrix} \dot{\theta} & \dot{\phi}\ \cos(\theta) & -\dot{\phi}\ \sin(\theta) \end{bmatrix}^{\intercal} \tag{1} $$

$$ {}^{\mathbf{P}}\vec{\omega}_{\mathbf{P}} = \begin{bmatrix} \dot{\beta} + \dot{\theta} & \dot{\phi}\ \cos(\beta + \theta) & -\dot{\phi}\ \sin(\beta + \theta) \end{bmatrix}^{\intercal} \tag{2} $$

https://doi.org/10.1017/S0263574726103464 Published online by Cambridge University Press

$$ {}^{\mathbf{H}}\vec{\omega}_{\mathbf{H}} = \begin{bmatrix} \dot{\theta}\,\cos(\psi) + \dot{\phi}\,\cos(\theta)\,\sin(\psi) \\ \dot{\phi}\,\cos(\psi)\,\cos(\theta) - \dot{\theta}\,\sin(\psi) \\ \dot{\psi} - \dot{\phi}\,\sin(\theta) \end{bmatrix} \tag{3} $$

The position vector corresponding to the center of mass of the yoke ($\mathbf{Y}_c$) and the hull ($\mathbf{H}_c$) as well as the origin of the pendulum frame ($\mathbf{P}_o$) are

$$ {}^{\mathbf{G}}_{\mathbf{G}}\vec{r}_{\mathbf{Y}_c} = {}^{\mathbf{G}}_{\mathbf{G}}\vec{r}_{\mathbf{H}_c} = {}^{\mathbf{G}}_{\mathbf{G}}\vec{r}_{\mathbf{P}_o} = \begin{bmatrix} X & r_h & Z \end{bmatrix}^{\mathsf{T}} \tag{4} $$

where X and Z are the coordinates of the hull center along the global frame $\mathbf{G}(OXYZ)$, and r_h is the radius of the sphere. Note that the origins of frames **Y, P, H** coincide at the center of the robot. The position vector corresponding to the pendulum's center of mass is given by:

$$ {}^{\mathbf{G}}_{\mathbf{G}}\vec{r}_{\mathbf{P}_c} = {}^{\mathbf{G}}_{\mathbf{P}}\vec{r}_{\mathbf{P}_c} + {}^{\mathbf{G}}_{\mathbf{G}}\vec{r}_{\mathbf{P}_o} \tag{5} $$

$$ {}^{\mathbf{G}}_{\mathbf{P}}\vec{r}_{\mathbf{P}_c} = {}^{\mathbf{G}}\mathbf{R}_{\mathbf{P}}\,{}^{\mathbf{P}}_{\mathbf{P}}\vec{r}_{\mathbf{P}_c} \text{ and } {}^{\mathbf{P}}_{\mathbf{P}}\vec{r}_{\mathbf{P}_c} = \begin{bmatrix} 0 & -r_p & 0 \end{bmatrix}^{\mathsf{T}} \tag{6} $$

where $\mathbf{P}_c$ stands for the pendulum's center of mass, and r_p is the distance between $\mathbf{P}_c$ and $\mathbf{P}_o$. Differentiating the position vectors, the linear velocities of the center of mass of the hull ($\mathbf{H}_c$), yoke ($\mathbf{Y}_c$), and pendulum ($\mathbf{P}_c$) are obtained as:

$$ {}^{\mathbf{G}}\vec{v}_{\mathbf{H}_c} = {}^{\mathbf{G}}\vec{v}_{\mathbf{Y}_c} = \begin{bmatrix} \dot{X} & 0 & \dot{Z} \end{bmatrix}^{\mathsf{T}} \tag{7} $$

$$ {}^{\mathbf{G}}\vec{v}_{\mathbf{P}_c} = \begin{bmatrix} \dot{X} \\ 0 \\ \dot{Z} \end{bmatrix} + {}^{\mathbf{G}}\vec{\omega}_{\mathbf{P}} \times {}^{\mathbf{G}}\mathbf{R}_{\mathbf{P}} \begin{bmatrix} 0 \\ -r_p \\ 0 \end{bmatrix} \tag{8} $$

The kinetic energy of the system can then be written as:

$$ \begin{aligned} K &= K_L + K_A, \\ K_L &= \frac{1}{2}\left(m_h \left\| {}^{\mathbf{G}}\mathbf{v}_{\mathbf{H}_c} \right\|^2 + m_y \left\| {}^{\mathbf{G}}\mathbf{v}_{\mathbf{Y}_c} \right\|^2 + m_p \left\| {}^{\mathbf{G}}\mathbf{v}_{\mathbf{P}_c} \right\|^2 \right), \\ K_A &= \frac{1}{2}\left({}^{\mathbf{H}}\boldsymbol{\omega}_{\mathbf{H}}^{\mathsf{T}}\, {}^{\mathbf{H}}I_{\mathbf{H}}\, {}^{\mathbf{H}}\boldsymbol{\omega}_{\mathbf{H}} + {}^{\mathbf{Y}}\boldsymbol{\omega}_{\mathbf{Y}}^{\mathsf{T}}\, {}^{\mathbf{Y}}I_{\mathbf{Y}}\, {}^{\mathbf{Y}}\boldsymbol{\omega}_{\mathbf{Y}} + {}^{\mathbf{P}}\boldsymbol{\omega}_{\mathbf{P}}^{\mathsf{T}}\, {}^{\mathbf{P}}I_{\mathbf{P}}\, {}^{\mathbf{P}}\boldsymbol{\omega}_{\mathbf{P}} \right). \end{aligned} \tag{9} $$

where m_j denotes the mass of body $\mathbf{J}$, and ${}^{\mathbf{J}}I_{\mathbf{J}}$ denotes the mass moment of inertia matrix of body $\mathbf{J}$ expressed in its own reference frame. The spherical robot can be represented in an ideal way as a combination of primitive objects. The hull can be assumed to be a hollow sphere, the yoke to a disc, and the pendulum to a rod, with uniform distribution of mass. Following these assumptions,

$$ {}^{\mathbf{H}}I_{\mathbf{H}} = \mathrm{diag}(I_h, I_h, I_h), \quad {}^{\mathbf{Y}}I_{\mathbf{Y}} = \mathrm{diag}(I_y, 2I_y, I_y), \quad {}^{\mathbf{P}}I_{\mathbf{P}} = \mathrm{diag}(I_p, 0, I_p), $$

where

$$ I_h = \frac{2}{3}m_h r_h^2, \quad I_y = \frac{1}{4}m_y r_h^2, \quad I_p = \frac{1}{3}m_p r_p^2. $$

From this we get the following upon expanding K_L and K_A as:

$$ \begin{aligned} K_L &= \frac{1}{2}(m_h + m_y + m_p)(\dot{x}^2 + \dot{z}^2) + \frac{1}{2}m_p r_p^2 \left(\dot{\phi}^2 \sin^2(\theta + \beta) + (\dot{\theta} + \dot{\beta})^2 \right) \\ &\quad - m_p r_p \left(\dot{x}\frac{d}{dt}\big(\sin(\theta + \beta)\sin\phi\big) + \dot{z}\frac{d}{dt}\big(\sin(\theta + \beta)\cos\phi\big) \right), \\ K_A &= \frac{1}{2}\Big[\left(\dot{\theta}^2 + \dot{\phi}^2 + \dot{\psi}^2 - 2\dot{\phi}\dot{\psi}\sin\theta \right) I_h \\ &\quad + \left(\dot{\theta}^2 + \dot{\phi}^2(1 + \cos^2\theta) \right) I_y + \left((\dot{\theta} + \dot{\beta})^2 + \dot{\phi}^2 \sin^2(\theta + \beta) \right) I_p \Big]. \end{aligned} \tag{10} $$

https://doi.org/10.1017/S0263574726103464 Published online by Cambridge University Press

The Potential Energy of the system is given by

$$\begin{aligned} V &= m_p g \left({}^{\mathbf{G}}_{\mathbf{P}}\vec{\mathbf{r}}_{\mathbf{P}_c} \cdot [0\ 1\ 0]^\intercal \right) + m_y g \left({}^{\mathbf{G}}_{\mathbf{Y}}\vec{\mathbf{r}}_{\mathbf{Y}_c} \cdot [0\ 1\ 0]^\intercal \right) \\ &= -r_p m_p g \cos(\theta + \beta). \end{aligned} \tag{11}$$

where the datum point for potential energy is chosen as the geometric center of the sphere.

In order to conduct a simulation, specific values have been assigned to the mass and dimensions of the hull, pendulum, and yoke. The mass of the hull has been set at 800 g, the mass of the pendulum at 200 g, and the mass of the yoke at 550 g. Similarly, the radius of the hull has been set to 12 cm, and the length of the pendulum has been set to 10 cm. These values have been chosen as inputs for the simulation to model as a representation of the prototype available in the lab on which previous experiments have been run. They have only been chosen to quantify the model, and the controller design isn't limited to them. A mass and dimension optimization can be done as a future scope of this work, as it has no effect on the derivation of the mathematical model.

2.3. Non-holonomic constraints

The constraint of rolling without slipping is non-holonomic and is given by

$${}^{\mathbf{G}}\vec{v}_{\mathbf{H}} = {}^{\mathbf{G}}\vec{\omega}_{\mathbf{H}} \times {}^{\mathbf{G}}\vec{r}_{\mathbf{H}} \tag{12}$$

where ${}^{\mathbf{G}}\vec{r}_{\mathbf{H}} = \begin{bmatrix} 0 & r_h & 0 \end{bmatrix}^\intercal$ denotes the vector (written in the global frame) between the stationary point on the hull, which is in contact with the ground and the sphere center. Eq. (12) is simplified further as

$$\dot{X} = r_h(\dot{\theta} \sin(\phi) - \dot{\psi} \cos(\phi) \cos(\theta)) \tag{13}$$

$$\dot{Z} = r_h(\dot{\theta} \cos(\phi) + \dot{\psi} \sin(\phi) \cos(\theta)) \tag{14}$$

These constraint equations are written in the form

$$a_1^\intercal \cdot \dot{q} = 0, \quad a_2^\intercal \cdot \dot{q} = 0 \tag{15}$$

where generalized coordinates $q = \begin{bmatrix} X & Z & \phi & \theta & \psi & \beta \end{bmatrix}^\intercal$, $\vec{a}_1$ & $\vec{a}_2$ are:

$$\vec{a}_1 = \begin{bmatrix} 1 & 0 & 0 & -r_h sin(\phi) & r_h cos(\phi)\, cos(\theta) & 0 \end{bmatrix}^\intercal \tag{16}$$

$$\vec{a}_2 = \begin{bmatrix} 0 & 1 & 0 & -r_h cos(\phi) & -r_h sin(\phi)\, cos(\theta) & 0 \end{bmatrix}^\intercal \tag{17}$$

Next, the Lagrangian model is formulated utilizing the deduced constraints.

2.4. Lagrange D'Alembert equations

The Lagrange D'Alembert equations for non-holonomic systems are given by

$$\begin{aligned} \frac{d}{dt}\left(\frac{\partial L}{\partial \dot{q}}\right) - \frac{\partial L}{\partial q} &= Q + \lambda_1 a_1 + \lambda_2 a_2, \\ Q &= \begin{bmatrix} 0 & 0 & 0 & 0 & T_s & T_p \end{bmatrix}^\intercal, \\ L &= K_L + K_A - V \\ q &= \begin{bmatrix} X & Z & \phi & \theta & \psi & \beta \end{bmatrix}^\intercal \end{aligned} \tag{18}$$

where T_s is the torque for forward rolling motion, and T_p is the torque on the pendulum. λ_1, λ_2 are Lagrange multipliers; a_1, a_2 come from simplifying Eq. (15). Given that none of K_L, K_A, and V are functions of x or z, and using Eqs. (13) and (14), we can break up Eq. (18) for each state q into the following:

https://doi.org/10.1017/S0263574726103464 Published online by Cambridge University Press

$$\begin{aligned} \frac{\partial L}{\partial x} = 0, \qquad & \frac{\partial L}{\partial z} = 0, \\ \implies \frac{d}{dt}\left(\frac{\partial L}{\partial \dot{x}}\right) = \lambda_1, \quad & \frac{d}{dt}\left(\frac{\partial L}{\partial \dot{z}}\right) = \lambda_2 \end{aligned} \tag{19}$$

Using Eq. (19), we can eliminate λ_1, λ_2 in the following equations.

$$\frac{d}{dt}\left(\frac{\partial L}{\partial \dot{\beta}}\right) - \frac{\partial L}{\partial \beta} = T_p, \tag{20}$$

$$\frac{d}{dt}\left(\frac{\partial L}{\partial \dot{\theta}}\right) - \frac{\partial L}{\partial \theta} = -r_h\left(sin(\phi)\lambda_1 + cos(\phi)\lambda_2\right), \tag{21}$$

$$\frac{d}{dt}\left(\frac{\partial L}{\partial \dot{\psi}}\right) - \frac{\partial L}{\partial \psi} = T_s + r_h cos(\theta)\left(cos(\phi)\lambda_1 - sin(\phi)\lambda_2\right), \tag{22}$$

$$\frac{d}{dt}\left(\frac{\partial L}{\partial \dot{\phi}}\right) - \frac{\partial L}{\partial \phi} = 0, \tag{23}$$

Finally, the last two equations of motion come from the Eqs. (13) and (14) as shown below:

$$\frac{d}{dt}\left(a_1^{\intercal} \cdot \dot{q}\right) = 0, \qquad \frac{d}{dt}\left(a_2^{\intercal} \cdot \dot{q}\right) = 0 \tag{24}$$

The system model that is formed using the Eqs. (20) to (24) can be represented as,

$$\mathbf{M}(q)\ddot{\mathbf{q}} + \mathbf{C}(q, \dot{q})\dot{\mathbf{q}} + \mathbf{g}(q) = \boldsymbol{\tau}, \tag{25}$$

where $\mathbf{M}(q)$, $\mathbf{C}(q, \dot{q})$, $\mathbf{g}(q)$, and $\boldsymbol{\tau}$ are expanded in the Appendix (Section 7.1). Using elementary row operations on Eq. (25) expanded in the Appendix (Section 7.2) and representing the state vector $\mathbf{x}$ and control inputs $\mathbf{u}$ compactly as

$$\mathbf{x} = \begin{bmatrix} \phi & \theta & \psi & \beta & X & Z & \dot{\phi} & \dot{\theta} & \dot{\psi} & \dot{\beta} & \dot{X} & \dot{Z} \end{bmatrix}^{\intercal}, \quad \mathbf{u} = \begin{bmatrix} T_s & T_p \end{bmatrix}^{\intercal}. \tag{26}$$

Eq. (25) can be simplified to give the control-affine form represented below:

$$\dot{\mathbf{x}} = \mathbf{f}(\mathbf{x}) + \mathbf{G}(\mathbf{x})\mathbf{u}, \tag{27}$$

where

$$\mathbf{f}(\mathbf{x}) = \begin{bmatrix} \dot{\phi} \\ \dot{\theta} \\ \dot{\psi} \\ \dot{\beta} \\ \dot{X} \\ \dot{Z} \\ f_7(\theta, \beta, \dot{\phi}, \dot{\theta}, \dot{\psi}, \dot{\beta}) \\ f_8(\theta, \beta, \dot{\phi}, \dot{\theta}, \dot{\psi}, \dot{\beta}) \\ f_9(\theta, \beta, \dot{\phi}, \dot{\theta}, \dot{\psi}, \dot{\beta}) \\ f_{10}(\theta, \beta, \dot{\phi}, \dot{\theta}, \dot{\psi}, \dot{\beta}) \\ f_{11}(\phi, \theta, \beta, \dot{\phi}, \dot{\theta}, \dot{\psi}, \dot{\beta}) \\ f_{12}(\phi, \theta, \beta, \dot{\phi}, \dot{\theta}, \dot{\psi}, \dot{\beta}) \end{bmatrix}, \quad \mathbf{G}(\mathbf{x}) = \begin{bmatrix} 0 & 0 \\ 0 & 0 \\ 0 & 0 \\ 0 & 0 \\ 0 & 0 \\ 0 & 0 \\ G_{7,1}(\theta, \beta) & 0 \\ 0 & G_{8,2}(\theta, \beta) \\ G_{9,1}(\theta, \beta) & 0 \\ 0 & G_{10,2}(\theta, \beta) \\ G_{11,1}(\phi, \theta, \beta) & G_{11,2}(\phi, \theta, \beta) \\ G_{12,1}(\phi, \theta, \beta) & G_{12,2}(\phi, \theta, \beta) \end{bmatrix}.$$

Expanding each term of this model equation becomes very lengthy and reduces the readability of this article; hence, a detailed representation of the methodology is given in the appendix. This model exhibits coupling between the forward rolling and steering motions of the robot. The forward rolling motion is characterized by the forward spin angle ψ and the heading angle ϕ, while the steering motion is characterized by the lean angle θ and the pendulum angle β.

https://doi.org/10.1017/S0263574726103464 Published online by Cambridge University Press

Analyzing the model equations reveals that the derivatives $\dot{\psi}$ and $\dot{\phi}$ appear in the expressions for the second derivatives $\ddot{\theta}$ and $\ddot{\beta}$. This indicates that the steering motion depends on the current rates of change of the forward spin and heading angles. Conversely, the variables θ, β, and their derivatives appear in the equations for $\ddot{\psi}$ and $\ddot{\phi}$, showing that the forward motion is influenced by the lean and pendulum angles and their rates of change. Therefore, changes in the forward motion variables ψ and ϕ impact the steering variables θ and β, and vice versa.

Finally, note that the system is underactuated with only two control inputs, T_s and T_p, which limits the number of outputs that can be controlled.

2.5. Rolling with slipping

The deduced constraints in the previous subsection enforce that the hull of the robot rolls on the ground without slipping. However, this is idealistic; therefore, we have generalized this setup to rolling with slipping as well. The generalized force vector when considering friction as an external force is as follows:

$$Q_{slip} = \begin{bmatrix} f_x \\ f_z \\ 0 \\ -r_h(f_x sin(\phi) + f_z cos(\phi)) \\ T_s - r_h cos(\theta)(f_x cos(\phi) - f_z sin(\phi)) \\ T_p \end{bmatrix} \tag{28}$$

Where f_x and f_z are the components of the friction force acting in the global X and Z directions, respectively, and T_s and T_p are the torques from the motors contributing to the forward angular velocity and the pendulum steering, respectively. From the Lagrangian formulation, we can deduce the values of λ_1 and λ_2 to be f_x and f_z, respectively.

Rolling with Slip may occur when the point of contact between the robot and the ground has relative motion between them or the force of friction required to maintain rolling is too high for the given surface. The friction model used for these simulations is the Coulomb friction model, and we demonstrate the effect of different coefficients of friction μ.

$$F_{Coulumb} = \mu \times F_{Normal} \times sign(v_{poc})$$

As we will see in Section 3, the system in steady-state circular motions stays well within the Coulomb model limit (μF_{Normal}), and we will specifically study the robustness of the wobble controller designed in Section 4 to the case of slipping at low speeds, expressed in Figure 5b.

2.6. System response for a circular motion

The dynamics of the spherical robot described in Section 2.4 are simulated using the ODE15s solver built into MATLAB. Specifically, we have simulated the steady-state behavior of the robot rolling along a circular path. This configuration is attained when the pendulum's angle and the robot's forward speed are held constant and the remaining state variables are initialized as zero.

Our system analysis is conducted for relatively smaller pendulum angles so that the robot does not lean excessively during steering motion. A steep lean angle during the steering motion would laterally tilt the camera mounted on the robot. Hence, we focus our analysis on a pendulum's swing of about 0° to 15° since this is a relatively small inclination. Within this range, simulations are roughly divided into two groups: Low Pendulum Angle (5°) and High Pendulum Angle (15°).

We have also classified the speeds of robot operation as either "Low Speed" or "High Speed." In Figure 4, we show the system response for the robot's center of mass as it moves forward at varying speeds while maintaining a pendulum angle of 15°. The circular paths that the robot follows are slightly

https://doi.org/10.1017/S0263574726103464 Published online by Cambridge University Press

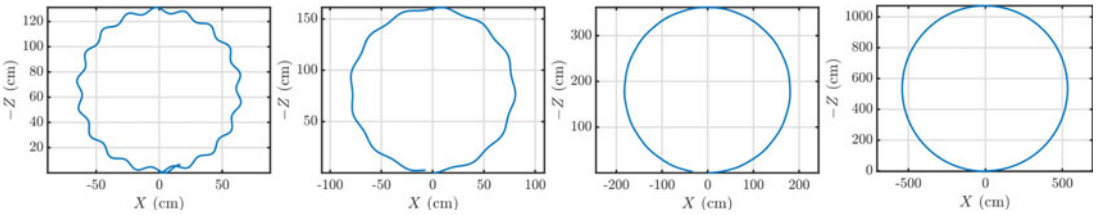


Figure 4. *Path followed by robot's COM while moving forward at different speeds* $|\dot{\psi}|$ *with* $\beta = 15°$.

wobbly due to oscillations in the robot's lean angle θ. The deviations from a perfect circular path shown in Figure 4 are proportional to the amplitude of oscillations in lean angle.

We can see from Figure 4 that the robot's wobbling is minimal when it is moving at a speed of 10 radians per second. At this speed, the robot follows a nearly smooth circular trajectory, as shown in Figure 5d. The magnitude of the mean value and amplitude of the lean angle is 1.76° for this case, which results in a total lean angle deviation of about 3.5° about the mean position. As this deviation is smaller than 5.73° (i.e. 0.1 rad), we can consider it to be a very small angular deviation. Therefore, for our simulations, we classify 10 radians per second as a high speed, as it results in relatively smaller values of wobbling.

Similarly, we classify 1 rad/s as a low speed because the effect of wobbling caused by center of mass perturbation is clearly visible in Figure 4. In this case, the corresponding behavior of lean angle (θ) is shown in Figure 5b, where the magnitude of the mean value and amplitude of the lean angle is 13.8°. This results in a total lean angle deviation of 27.62° about the mean position, which is very high. Such a high deviation can result in significantly shaky camera feedback, which is not desirable. Additionally, this deviation is well above the approximate small angle value of 20°, where small angle approximations are approximately valid.

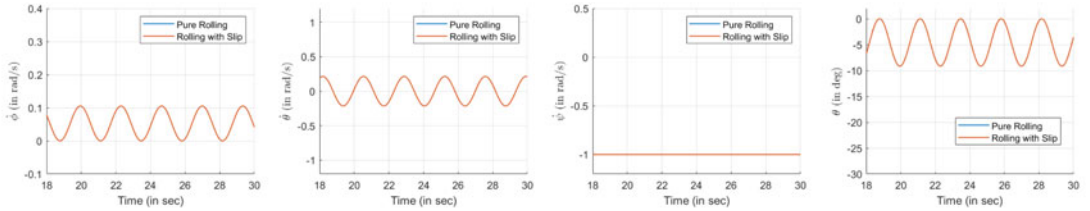
We further investigate the system response for the rate of change of heading angle $\dot{\phi}$, rate of change of lean angle $\dot{\theta}$, forward speed $\dot{\psi}$, and lean angle θ by simulating the steady state circular motion of the robot with the following four configurations of pendulum angle β and forward rolling speed $|\dot{\psi}|$ while in pure rolling as well as rolling with slip:

	Configurations	
	Low pendulum angle ($\beta = 5°$)	High pendulum angle ($\beta = 15°$)
Low Speed ($\|\dot{\psi}\| = 1$ rad/s)	Figure 5a	Figure 5b
High speed ($\|\dot{\psi}\| = 10$ rad/s)	Figure 5c	Figure 5d

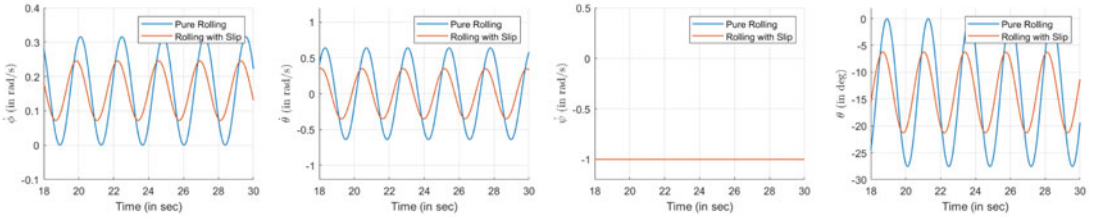
In order to facilitate the comparison of the figures, we have opted to use different scales for certain variables in each case. We kept a consistent scale for the θ variable over time, as this allowed for a relative comparison of the wobble values depicted in Figure 5a, 5b, 5c, and 5d. In each figure set, we scaled $\dot{\phi}$, $\dot{\theta}$, and $\dot{\psi}$ in the same way to enable a relative comparison of the angular velocities.

The system response in the figures shows two distinct ends. On one end, we see the lean angle exceeding the range in which it can be approximated as a small angle. For instance, at a rolling speed of 1 rad/sec and a pendulum angle of 15°, the lean angle can reach up to 30° in magnitude. If we were to go further on these sides of the configurations, the wobble would increase further. If the robot were to operate at speeds below 1 rad/s with the pendulum at a reasonable angle of 15°, it would cause an excessive tilt angle, with values exceeding 30°. This high tilt angle would cause the camera to tilt excessively in the sideways direction, resulting in a loss of camera field of view on the other side.

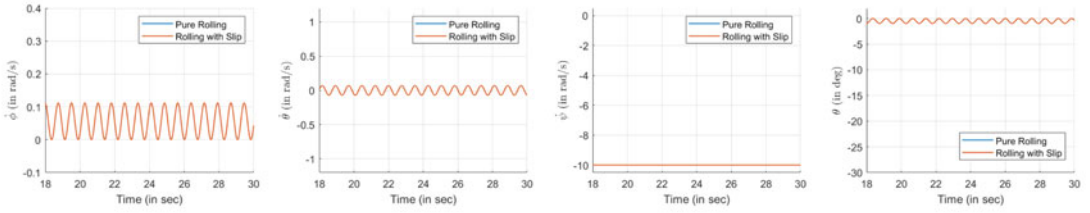
https://doi.org/10.1017/S0263574726103464 Published online by Cambridge University Press



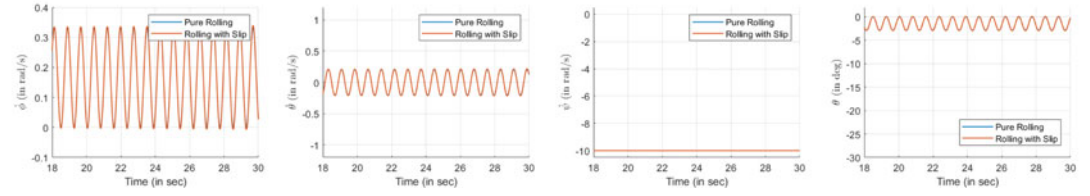
(a) System response at $\beta = 5°$ and $|\dot{\psi}| = 1$ rad/s (low speed)



(b) System response at $\beta = 15°$ and $|\dot{\psi}| = 1$ rad/s (low speed)



(c) System response at $\beta = 5°$ and $|\dot{\psi}| = 10$ rad/s (high speed)



(d) System response at $\beta = 15°$ and $|\dot{\psi}| = 10$ rad/s (high speed)

Figure 5. *System response at various pendulum angles and forward speeds.*

On the other end of the system response, we observe cases where the lean angle lies within the range of small angle approximations. For example, at a rolling velocity of 10 rad/sec and a pendulum angle of 5°, the value of lean angle is much smaller than 0.1 rad (i.e., 5.73°), making it very small. We can also observe that the rest of the system response is not as highly non-linear as when lean angles are on the high end, as observed in Figure 5b. For the purposes of this work, we would approximate angles less than 0.35 rad (i.e., 20°) as small angles so that higher orders of these angles can be neglected.

In system responses where the lean angle falls within the small angle approximation range, we can observe the following characteristics:

- The magnitudes of $\dot{\phi}\dot{\theta}$, $\dot{\phi}^2$, and $\dot{\theta}^2$ are at least one order of magnitude smaller than that of $\dot{\psi}$, as shown in Figure 5a, 5c, and 5d.
- The value of $\dot{\psi}$ remains within a 1-2% deviation from the mean value, as shown in Figure 5a, 5c, and 5d.

https://doi.org/10.1017/S0263574726103464 Published online by Cambridge University Press

3. Steady-state analysis of wobbly circular motion

In this section, we aim to simplify and linearize the dynamics of the circular steady-state motion for the system configurations where the lean angle falls within the range of small-angle approximations, as discussed in Section 2.6.

This leads to the development of expressions for wobble amplitude, wobble frequency, precession rate, and radius of curvature. Then, the system response of the original system is compared to the system response of the simplified system.

3.1. Model simplification

The 3D mathematical model presented in the Section 2 for the robot is characterized by its high complexity and nonlinearity. However, in order to derive characteristics of a wobbly circular motion, we can make a few intuitive assumptions. Note that these assumptions are only valid as long as we follow the circular motion analysis, and these equations derived will hold for the results discussed in Section 3. We can assume that the pendulum angle β is maintained at a constant value, with negligible angular velocity ($\dot{\beta} \approx 0$) and angular acceleration ($\ddot{\beta} \approx 0$). Consequently, the original Eqs. (21), (22), and (23) can be reduced to the following three equations:

$$\begin{aligned}
&\left[I_h + (m_p + m_y + m_h) r_h^2 \cos^2(\theta)\right] \ddot{\psi} - \left[\frac{(m_p + m_y + m_h) r_h^2}{2} \sin(2\theta)\right] \dot{\psi}\dot{\theta} \\
&- \left[I_h \cos(\theta) + (m_p + m_y + m_h) r_h^2 \cos(\theta) - 2 m_p r_p r_h \cos(\beta) \cos^2(\theta) + 2 m_p r_p r_h \sin(\beta) \cos(\theta) \sin(\theta)\right] \dot{\phi}\dot{\theta} \\
&- \left[I_h \sin(\theta) - m_p r_p r_h \sin(\beta) \cos^2(\theta) - m_p r_p r_h \cos(\beta) \cos(\theta) \sin(\theta)\right] \ddot{\phi} = 0
\end{aligned} \tag{29}$$

$$\begin{aligned}
&\left[I_p + I_h + I_y + m_p r_p^2 + (m_p + m_y + m_h) r_h^2 - 2 m_p r_p r_h \cos(\beta + \theta)\right] \ddot{\theta} + \left[m_p r_p r_h \sin(\beta + \theta)\right] \dot{\theta}^2 \\
&+ \left[I_h \cos(\theta) + (m_p + m_y + m_h) r_h^2 \cos(\theta) - \frac{m_p r_p r_h}{2} (\cos(\beta + 2\theta) + \cos(\beta))\right] \dot{\phi}\dot{\psi} + m_p r_p g \sin(\beta + \theta) \\
&+ \left[\frac{I_y \sin(2\theta)}{2} - \frac{I_p \sin(2\beta + 2\theta)}{2} - \frac{m_p r_p^2 \sin(2\beta + 2\theta)}{2} + m_p r_p r_h \sin(\beta + \theta)\right] \dot{\phi}^2 = 0
\end{aligned} \tag{30}$$

$$\begin{aligned}
&\left[I_h + \frac{I_p}{2} + \frac{3 I_y}{2} + \frac{I_y \cos(2\theta)}{2} - \frac{I_p \cos(2\beta + 2\theta)}{2} + \frac{m_p r_p^2}{2} (1 - \cos(2\beta + 2\theta))\right] \ddot{\phi} - \left[I_h \sin(\theta)\right. \\
&\left. - \frac{m_p r_p r_h}{2} (\sin(\beta) + \sin(\beta + 2\theta))\right] \ddot{\psi} - \left[I_h \cos(\theta) - \frac{m_p r_p r_h}{2} (\cos(\beta + 2\theta) - \cos(\beta))\right] \dot{\psi}\dot{\theta} \\
&- \left[I_y \sin(2\theta) - I_p \sin(2\beta + 2\theta) - m_p r_p^2 \sin(2\beta + 2\theta) + m_p r_p r_h \sin(\beta + \theta)\right] \dot{\phi}\dot{\theta} = 0
\end{aligned} \tag{31}$$

The mathematical model of the system, described by Eqs. (29), (30), and (31), encompasses all pendulum angles and forward speeds. These equations can be further simplified based on the configuration outlined in Section 2.6. This configuration ensures that the robot rolls along a circular path, exhibiting small-angle oscillations, preventing excessive tilting that could obstruct the camera's field of view. Section 2.6 elaborates on the conditions necessary for this particular configuration, which can be summarized as follows:

- Pendulum angle β is small in magnitude ($\sin\beta \approx \beta$ and $\cos\beta \approx 1$).
- Lean angle θ is small in magnitude ($\sin\theta \approx \theta$ and $\cos\theta \approx 1$).
- Forward speed $\dot{\psi}$ is constant.

https://doi.org/10.1017/S0263574726103464 Published online by Cambridge University Press

- $\dot{\psi}$ is larger than $\dot{\phi}$ and $\dot{\theta}$. Hence $\dot{\phi}\dot{\theta}$, $\dot{\phi}^2$, $\dot{\theta}^2$ can be neglected in comparison to $\dot{\psi}$.

These conditions are used to further simplify Eqs. (29), (30), and (31) to give:

$$\ddot{\psi} = 0 \tag{32}$$

$$\left[I_p + I_h + I_y + m_p r_p^2 + (m_p + m_y + m_h) r_h^2 - 2m_p r_p r_h\right]\ddot{\theta} + \left[I_h + (m_p + m_y + m_h) r_h^2 - m_p r_p r_h\right]\dot{\phi}\dot{\psi} + m_p r_p g(\beta + \theta) = 0 \tag{33}$$

$$\ddot{\phi} = \frac{I_h}{I_h + 2I_y}\dot{\psi}\dot{\theta} \tag{34}$$

3.2. Formulation of circular motion characteristics

A spherical robot's circular motion characteristics include precession rate, wobble amplitude, wobble frequency, and radius of curvature. The expressions for these quantities can now be obtained using the simplified model.

Precession rate Using constant $\dot{\psi}$, Eqn. (34) can be integrated to obtain $\dot{\phi}$.

$$\dot{\phi} = \frac{I_h}{I_h + 2I_y}\dot{\psi}\theta + c \tag{35}$$

where c is a constant of integration. We assume that the robot starts with initial θ and $\dot{\phi} = 0$, which gives $c = 0$.

Wobbling From Eqs. (33) and (35), we get

$$\left[I_p + I_h + I_y + m_p r_p^2 + (m_p + m_y + m_h) r_h^2 - 2m_p r_p r_h\right]\ddot{\theta} + \left[\frac{I_h(I_h + (m_p + m_y + m_h) r_h^2 - m_p r_p r_h)}{I_h + 2I_y}\dot{\psi}^2 + m_p r_p g\right]\theta = -m_p r_p g\beta \tag{36}$$

Eq. (36) is a standard second-order equation, the solution of which is given by:

$$\theta = A(1 - \cos(\omega t)) \tag{37}$$

where A is the amplitude of oscillations and ω is the frequency of oscillations given by:

$$A = \frac{-m_p r_p g\beta}{\frac{I_h(I_h + (m_p + m_y + m_h) r_h^2 - m_p r_p r_h)}{I_h + 2I_y}\dot{\psi}^2 + m_p r_p g} \tag{38}$$

$$\omega = \sqrt{\frac{m_p r_p g + \frac{I_h(I_h + (m_p + m_y + m_h) r_h^2 - m_p r_p r_h)}{I_h + 2I_y}\dot{\psi}^2}{I_p + I_h + I_y + m_p r_p^2 + (m_p + m_y + m_h) r_h^2 - 2m_p r_p r_h}} \tag{39}$$

Radius of curvature For a sphere moving in a circular trajectory with pure rolling, the radius of curvature ρ can be approximated as

$$Time = \frac{2\pi}{\dot{\phi}_{mean}} = \frac{2\pi\rho}{\dot{\psi} r_h} \implies \rho = \frac{\dot{\psi} r_h}{\dot{\phi}_{mean}} \tag{40}$$

$$\rho = \frac{-r_h\left([I_h + (m_p + m_y + m_h) r_h^2 - m_p r_p r_h] I_h \dot{\psi}^2 + [I_h + 2I_y] m_p r_p g\right)}{m_p r_p g I_h \beta} \tag{41}$$

https://doi.org/10.1017/S0263574726103464 Published online by Cambridge University Press

The dynamics of the circular steady-state motion can be further simplified based on forward speed: low forward speeds and high forward speeds.

3.2.1. Low forward speeds

For forward speeds below 2.8 rad/s, the ratio of $r_h\dot{\psi}^2$ to g is smaller than one order of magnitude. As a result, the terms containing $r_h\dot{\psi}^2$ can be neglected when considering low forward speeds. This approximation greatly simplifies the Eqs. (38), (39), and (41), leading to the following expressions:

Wobbling The expressions for wobble amplitude and frequency become:

$$A = -\beta \tag{42}$$

$$\omega = \sqrt{\frac{m_p r_p g}{I_p + I_h + I_y + m_p r_p^2 + (m_p + m_y + m_h) r_h^2 - 2 m_p r_p r_h}} \tag{43}$$

Radius of curvature

$$\rho = \frac{-r_h (I_h + 2 I_y)}{I_h \beta} \tag{44}$$

3.2.2. Very high forward speeds

When the forward speeds exceed 28.6 rad/s, the ratio g to $\dot{\psi}$ becomes smaller than one order of magnitude. Therefore, for very high forward speeds, the terms containing g can be neglected, leading to a simplification of Eqs. (38), (39), and (41). Consequently, the following expressions can be obtained:

Wobbling The expressions for wobble amplitude and frequency become:

$$A = -\frac{(I_h + 2 I_y)(m_p r_p g)\beta}{I_h (I_h + (m_p + m_y + m_h) r_h^2 - m_p r_p r_h)\dot{\psi}^2} \tag{45}$$

$$\omega = \dot{\psi} \sqrt{\frac{I_h (I_h + (m_p + m_y + m_h) r_h^2 - m_p r_p r_h)}{(I_h + 2 I_y)(I_p + I_h + I_y + m_p r_p^2 + (m_p + m_y + m_h) r_h^2 - 2 m_p r_p r_h)}} \tag{46}$$

Radius of curvature

$$\rho = -\left(\frac{I_h + (m_p + m_y + m_h) r_h^2 - m_p r_p r_h}{m_p r_p g \beta} \right) r_h \dot{\psi}^2 \tag{47}$$

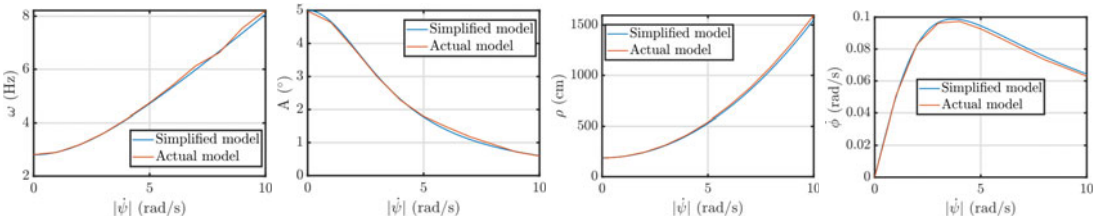
The Eq. (47) represents the radius of curvature at very high speeds and exhibits a similarity to the radius of curvature formulas found in existing literature [35, 36] across all speed ranges. However, it is important to note that these literature-based formulas do not offer a valid expression for the radius of curvature applicable to slower operational speeds of spherical robots.

3.3. Analysis of circular motion characteristics

In this section, we analyze the expressions of wobble amplitude Eq. (38) and frequency Eq. (39), precession rate Eq. (35), and radius of curvature Eq. (41), in detail. Our objective is to gain a comprehensive understanding of their characteristics and their dependence on key parameters, β and $\dot{\psi}$. Furthermore, we aim to compare these expressions with the system response obtained from the actual model Eq. (27).

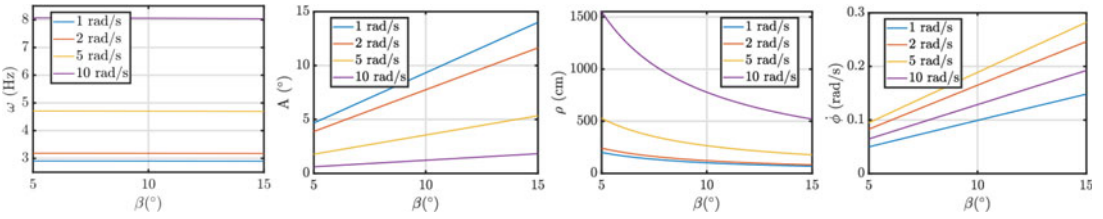
To carry out this analysis, we focus on the forward speed range spanning from 1 rad/s to 10 rad/s, as previously discussed in Section 2.6. By examining these aspects, we seek to deepen our insights into the behavior and performance of the system under investigation.

https://doi.org/10.1017/S0263574726103464 Published online by Cambridge University Press



(a) Wobble frequency (b) Wobble amplitude (c) Radius of curvature (d) Precession rate

Figure 6. *Circular motion characteristics vs forward speed $\dot{\psi}$ at a constant pendulum angle ($\beta = 5°$).*



(a) Wobble frequency (b) Wobble amplitude (c) Radius of curvature (d) Precession rate

Figure 7. *Circular motion characteristics vs pendulum angle β at different forward speeds $\dot{\psi}$.*

Wobbling The spherical robot's wobble or lateral oscillations are characterized by the lean angle θ. Based on the expression Eq. (37), θ is sinusoidal with oscillations centered away from the origin.

The relationship between wobble frequency and forward speed at a constant pendulum angle of 5° is depicted in Figure 6a. The wobble frequency is found to be nearly constant at low forward speeds. The figure also illustrates the similarity between the system response for wobble frequency generated by the actual model and the simplified model Eq. (39) at different speeds.

The relationship between wobble frequency and pendulum angle for a range of constant forward speeds is shown graphically in Figure 7a, which is based on Eq. (39). It can be inferred from the figure that for any constant forward speed, the wobble frequency is independent of the pendulum angle. We can also observe that the wobble frequency is greater at higher speeds for any given pendulum angle.

The relationship between wobble amplitude and forward speed for a constant pendulum angle of 5° is illustrated in Figure 6b. This figure demonstrates that the amplitude of oscillations in θ varies inversely with $\dot{\psi}^2$. The figure also illustrates the similarity between the system response for the amplitude of lateral oscillations generated by the actual model and the simplified model Eq. (38) at different speeds.

The relationship between wobble amplitude and pendulum angle for a range of constant forward speeds is shown graphically in Figure 7b, which is based on Eq. (38). For constant forward speed, the wobble amplitude is directly proportional to pendulum angle β. We can also observe that wobble amplitude decreases with increasing speed for any given pendulum angle.

Radius of curvature According to the Eq. (41), the radius of curvature depends on the angle of the pendulum and forward speed. If we control these two variables, we can indirectly affect the radius of curvature of the robot. This can facilitate the robot's movement along a curved path.

https://doi.org/10.1017/S0263574726103464 Published online by Cambridge University Press

In Figure 6c, we can observe the correlation between the radius of curvature and the forward speed, considering a fixed pendulum angle of 5°. At lower forward speeds, the radius of curvature remains relatively constant. However, as the forward speed increases, the radius of curvature demonstrates a direct proportionality to the square of the forward speed. Consequently, higher speeds result in a larger turning radius. Figure 6c also compares the radius of curvature values generated by the actual model with those generated by the simplified model (refer Eq. (41)).

The relationship between the radius of curvature and pendulum angle for a range of constant forward speeds is shown graphically in Figure 7c, which is based on Eq. (41). The radius of curvature is inversely proportional to the pendulum angle for constant forward speed. Therefore, the robot makes sharper turns as the pendulum tilts further. For any given pendulum angle, we can see that the radius of curvature increases as forward speed increases.

Precession rate The robot's precession rate indicates how quickly it completes one complete revolution as it rolls along a circular path. According to the Eq. (35), the magnitude of the precession rate is directly proportional to the lean angle. Consequently, the precession rate oscillates when the robot's motion involves lateral oscillations. This section analyzes the precession rate's mean value to comprehend its behavior in relation to forward velocity and pendulum angle.

The Figure 6d depicts the relationship between the mean precession rate and the forward speed when the pendulum angle is held constant at 5°. It is evident from the figure that the mean precession rate exhibits an increasing trend at lower forward speeds. However, as the forward speed continues to rise, the mean precession rate becomes inversely proportional to the rate of change of the pendulum angle. Eq. (40) describes the interplay among the precession rate, the radius of curvature, and forward speeds. At low speeds, where the radius of curvature remains relatively constant (see Figure 6c), we observe a direct relationship between the mean precession rate and the speed. As the speed increases, the mean precession rate shows a linear growth. However, when we consider higher speeds, the radius of curvature starts to increase at a non-linear rate. Consequently, the mean precession rate begins to decrease even though the speed continues to increase in a linear fashion. Figure 6d also illustrates the similarity between the system response for the mean precession rate generated by the actual model and the simplified model Eq. (35) at different speeds.

The relationship between the mean precession rate and pendulum angle for a range of constant forward speeds is shown graphically in Figure 7d, which is based on Eq. (35). The figure illustrates that the mean precession rate is directly proportional to the pendulum angle. However, when examining the effect of constant forward speeds on the mean precession rate, a notable observation emerges. It is evident that the mean precession rate does not consistently increase or decrease with speed for a specific pendulum angle.

4. Controller design

The spherical robot can be commanded to execute specific maneuvers, such as turning, by controlling the value of pendulum angle β, or forward speed, by controlling $\dot{\psi}$, in a teleoperation setup [7]. Controlling the robot's speed and pendulum angle, as discussed in Section 3.3, results in indirect control over the radius of curvature as per Eq. (41). It is evident from Section 2.6 that the robot does not move in an exact circular arc but rather wobbles. Therefore, it is necessary to stabilize this wobbly behavior, which

https://doi.org/10.1017/S0263574726103464 Published online by Cambridge University Press

is characterized by the oscillations of the lean angle θ. In this section, we present a controller design for semi-autonomous robot operation to achieve the following control objectives:

1. Heading control: Moving the robot along the desired curve or line by changing the turning radius
2. Wobble control: Limiting lateral oscillations to obtain sharp feedback from the robot's camera

For the robot's lateral oscillations to stabilize, the lean angle θ must remain fixed ($\dot{\theta}_{des} = 0$). To achieve heading control, the desired value of the pendulum's angle β_{des} would be determined based on the required radius of curvature for a given operational speed $\dot{\psi}$. The robot's $\dot{\psi}_{des}$ will be set according to the requirements of the teleoperator. For example, if careful surveillance is required, the teleoperator may need to move the robot slowly along a path. Rapidly reaching a destination may necessitate traveling at a faster rate. It should be noted that β_{des} should be small due to space constraints and the need to maintain the robot's upright position for enhanced camera coverage. The following sections describe the controller's strategy for achieving these objectives and the results it achieved.

4.1. Approach

With only two inputs, T_s and T_p, there are only two controllable quantities. Therefore, we can choose between the following outputs, which are related to forward rolling motion (speed) and steering (pendulum angle/lean angle rate):

$$\mathbf{y} = \begin{bmatrix} y_1 \\ y_2 \end{bmatrix} = \begin{bmatrix} \dot{\psi} \\ \beta \end{bmatrix} \text{ or } \mathbf{y} = \begin{bmatrix} y_1 \\ y_3 \end{bmatrix} = \begin{bmatrix} \dot{\psi} \\ \dot{\theta} \end{bmatrix} \tag{48}$$

Similar to input–output feedback linearization approach, we repeatedly differentiate the potential output functions y_1, y_2 and y_3 until the input $\mathbf{u}$ appears to obtain:

$$\begin{bmatrix} \dot{y}_1 \\ \ddot{y}_2 \\ \dot{y}_3 \end{bmatrix} = \begin{bmatrix} \ddot{\psi} \\ \ddot{\beta} \\ \ddot{\theta} \end{bmatrix} = \begin{bmatrix} f_9(\theta, \beta, \dot{\phi}, \dot{\theta}, \dot{\psi}, \dot{\beta}) \\ f_{10}(\theta, \beta, \dot{\phi}, \dot{\theta}, \dot{\psi}, \dot{\beta}) \\ f_8(\theta, \beta, \dot{\phi}, \dot{\theta}, \dot{\psi}, \dot{\beta}) \end{bmatrix} + \begin{bmatrix} G_{9,1}(\theta, \beta) & 0 \\ 0 & G_{10,2}(\theta, \beta) \\ 0 & G_{8,2}(\theta, \beta) \end{bmatrix} \begin{bmatrix} T_s \\ T_p \end{bmatrix} \tag{49}$$

It can be observed from Eq. (49) that $\ddot{\psi}$ depends only on T_s. Whereas $\ddot{\beta}$ and $\ddot{\theta}$ depend only on T_p.

As input T_s is exclusive to a particular output $\ddot{\psi}$, we design the speed control torque (T_s) separately using a proportional controller with high gain $K_{p,\dot{\psi}}$ as shown:

$$T_s = K_{p,\dot{\psi}}(\dot{\psi}_{des} - \dot{\psi}) \tag{50}$$

To control pendulum angle and wobble, the controller input T_p is designed as a linear combination of the required torques for β and $\dot{\theta}$ control. Let $T_{p,\beta}$ be the pendulum control torque required to maintain a β_{des}. Let $T_{p,\dot{\theta}}$ be the wobble control torque required to maintain $\dot{\theta}_{des} = 0$. Then a net torque T_p can be found as a weighted sum of wobble control torque ($T_{p,\dot{\theta}}$) and pendulum control torque ($T_{p,\beta}$) as shown:

$$T_p = \gamma T_{p,\dot{\theta}} + \delta T_{p,\beta} \tag{51}$$

Wobble control torque ($T_{p,\dot{\theta}}$) design: We implement the underlying concepts of input–output feedback linearization via static feedback to cancel nonlinear terms appearing in $\dot{y}_3$ and then apply a proportional controller term v_θ.

$$T_{p,\dot{\theta}} = \left[\frac{1}{G_{8,2}(\theta, \beta)} (-f_8(\theta, \beta, \dot{\phi}, \dot{\theta}, \dot{\psi}, \dot{\beta}) + v_\theta) \right] \text{ where } v_\theta = K_{p,\dot{\theta}}(\dot{\theta}_{des} - \dot{\theta}) \tag{52}$$

Pendulum control torque ($T_{p,\beta}$) design: We implement a combination of a feedback term v_β and a feedforward term to counteract gravitational torque. v_β consists of a proportional-derivative (PD) controller with high gains $K_{p,\beta}$ and $K_{d,\beta}$ as shown:

$$T_{p,\beta} = [m_p g r_p \sin(\beta + \theta) + v_\beta] \text{ where } v_\beta = K_{p,\beta}(\beta_{des} - \beta) + K_{d,\beta}(\dot{\beta}_{des} - \dot{\beta}) \tag{53}$$

https://doi.org/10.1017/S0263574726103464 Published online by Cambridge University Press

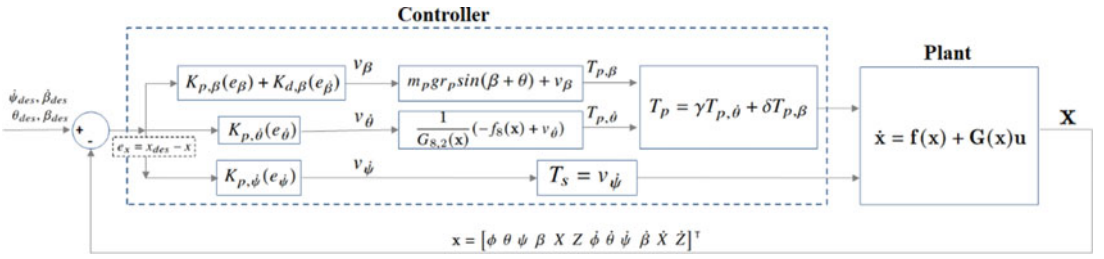


Figure 8. *Block diagram for controller design.*

The proposed controller architecture is shown in Figure 8. To ideally emulate our robot's actuation system, the speed gain $K_{p,\dot\psi}$ and pendulum gains $K_{p,\beta}$ and $K_{d,\beta}$ are chosen to be arbitrarily large. This represents the lower-level controller that controls the angular position of the pendulum and the speed of the motor driving the robot forward almost instantaneously. In contrast, the wobble control gain $K_{p,\dot\theta}$ is much smaller and empirically fine-tuned, since the proportional term v_θ in the wobble torque $T_{p,\dot\theta}$ does not compensate for the nonlinear and coupling terms of θ; these are instead canceled via input–output linearization. For the simulations, we use $K_{p,\dot\theta} = 25$, $K_{p,\beta} = 10^9$, $K_{d,\beta} = 5 \times 10^8$, and $K_{p,\dot\psi} = 10^9$, where the large pendulum and speed gains represent ideal servo-motors, while $K_{p,\dot\theta}$ sets the system's responsiveness to wobble induced by coupling and inertia.

To determine suitable values for the coefficients γ and δ, the T_p controller was implemented and evaluated under three distinct configurations. The first two correspond to limiting cases: pure pendulum control ($\gamma = 0, \delta = 1$) and pure oscillation control ($\gamma = 1, \delta = 0$). The third case combines both strategies by assigning intermediate values ($\gamma = 0.9, \delta = 0.1$), enabling the simultaneous regulation of both the pendulum and wobble control torques.

Before applying the controller, the robot is made to traverse a wobbly circular path at steady state for the initial five seconds, as discussed in Section 3. The corresponding radius of curvature is determined using Eq. (41), considering an initial pendulum angle of 15° and a forward speed $|\dot\psi| = 1$. The three control configurations are summarized below with reference to their system responses.

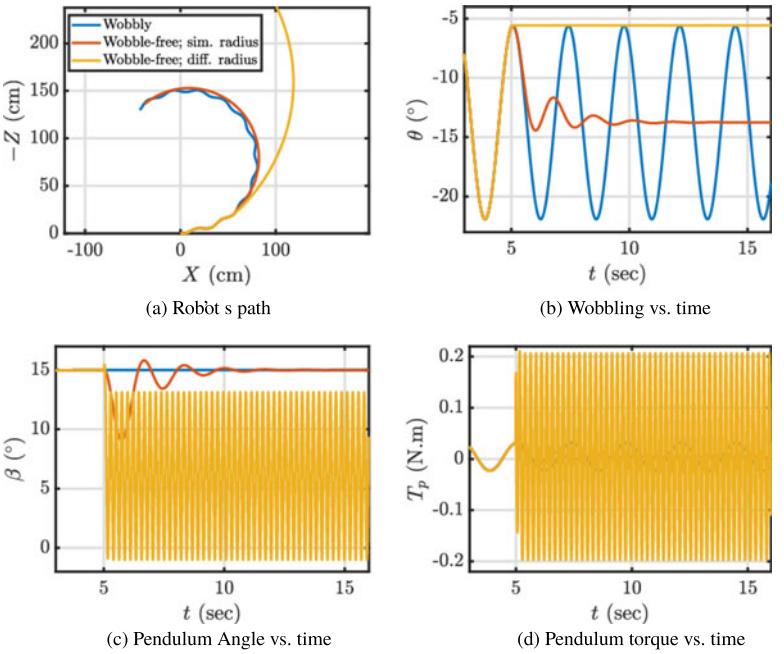
Case 1: Wobbly (Pendulum – only, $\gamma = 0, \delta = 1$) In this configuration, only the pendulum control torque ($T_{p,\beta}$) is active. The robot follows the desired curvature radius but exhibits pronounced oscillations in the lean angle θ, as shown in Figure 9b, with an amplitude of 8.18° and a mean of 13.74°. The pendulum angle β remains steady around 15°, as intended (Figure 9c).

Case 2: Wobble – free; different radius (Oscillation control, $\gamma = 1, \delta = 0$) Here, the wobble control torque component ($T_{p,\dot\theta}$) is applied to suppress oscillations. As observed in Figure 9b, the lean angle θ stabilizes to a mean of 5.56°, with the amplitude decaying to approximately $0.4° \times 10^{-6}$, indicating complete suppression of wobbling. However, the pendulum angle β exhibits high-frequency oscillations (amplitude 7.07°, mean 6.06°), leading to an increased radius of curvature (Figure 9a).

Case 3: Wobble – free; similar radius (Hybrid control, $\gamma = 0.9, \delta = 0.1$) This case integrates both control components ($T_{p,\beta}$ and $T_{p,\dot\theta}$), enabling the robot to maintain the desired curvature radius while minimizing wobbling. The lean angle θ settles to a steady-state mean of 13.75° with an oscillation amplitude of $1.2° \times 10^{-3}$a reduction of several orders of magnitude compared to the uncontrolled case. The pendulum angle β also remains stable near 15° (Figure 9c).

The configuration with $\gamma = 0.9$ and $\delta = 0.1$ thus achieves a stable, wobble-free motion while preserving the intended curvature, effectively balancing the objectives of both pendulum and oscillation control. A more formal optimization for tuning these parameters will be pursued in future work, particularly within the context of point-to-point navigation.

https://doi.org/10.1017/S0263574726103464 Published online by Cambridge University Press



(a) Robot s path (b) Wobbling vs. time

(c) Pendulum Angle vs. time (d) Pendulum torque vs. time

Figure 9. *System response by choosing different linear combinations of $\gamma T_{p,\dot{\theta}} + \delta T_{p,\beta}$ during a circular motion with $\beta_{des} = 15°$.*

4.2. Results

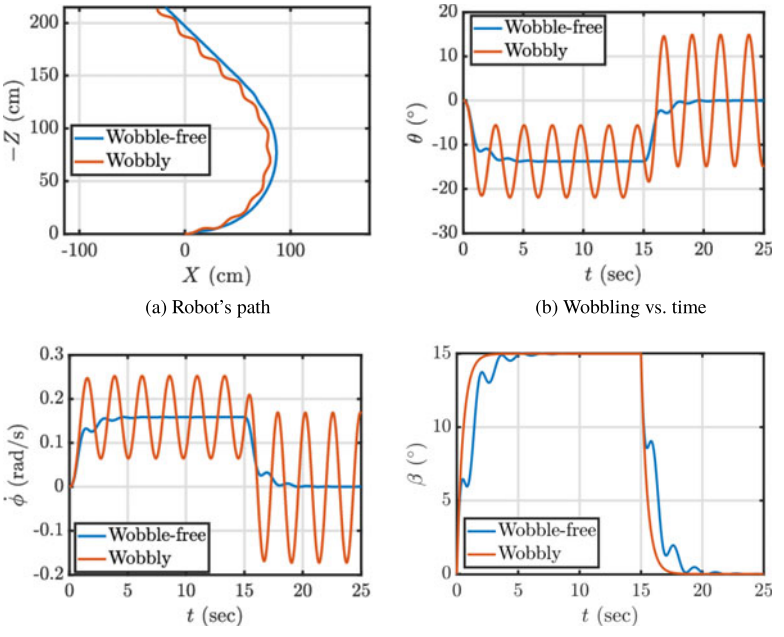
In this section, we present a comparison of the results obtained from implementing the linear combination torque T_p ($\gamma = 0.9$, $\delta = 0.1$) with the pendulum control torque $T_{p,\beta}$ in order to achieve a turning maneuver[1] for the robot as depicted in Figure 10. We also studied the robustness of this wobble controller to low coefficients of friction ($\mu = 0.01$) as depicted in Figure 11 and we see that the controller is able to eliminate lateral oscillations effectively even in the event of rolling with slip.

This study involves a simulated experiment, where we initially position the robot at the origin with a forward speed of $|\dot{\psi}| = 1$ rad/s. All other state variables are initialized to zero. To maintain the desired forward speed, we apply a speed controller T_s. Subsequently, we examine two distinct scenarios based on the torque applied to the system: the pendulum control torque ($T_{p,\beta}$) and the linear combination torque T_p. These scenarios result in a turning maneuver characterized by wobbling and wobble-free motion, respectively. During the initial 15 s of the simulation, we set the desired value of β to 15°. Throughout this duration, the robot executes a turning motion while rolling along a circular path. Following this initial period, we set the desired value of β to 0° for the remainder of the simulation. During this phase, the robot moves along a straight line.

Figure 10b vividly illustrates the elimination of wobble after a brief transient phase when the linear combination-based controller (T_p) is implemented. Comparing the first 15 s of motion, we observe a significant difference in the amplitude of oscillation in the lean angle θ between the case of wobbly motion (8.14°) and the wobble-free motion ($4.45° \times 10^{-4}$). In the wobble-free motion scenario, the lean angle θ stabilizes around a mean value of 13.76° during the turning phase, causing the robot to tilt towards the center of the turn. Subsequently, during the linear motion phase, θ converges to 0°, indicating that the robot successfully returns to an upright position upon completing the turning motion.

[1] The video at https://youtu.be/430yfKLEphw demonstrates the 3D multibody dynamic simulation of the pendulum-actuated spherical robot generated in Simulink using the VRML (Virtual Reality Modeling Language) functionality. We illustrate the controller design results in the video by contrasting the robot's wobbly and wobble-free turning maneuvers modeled in this study.

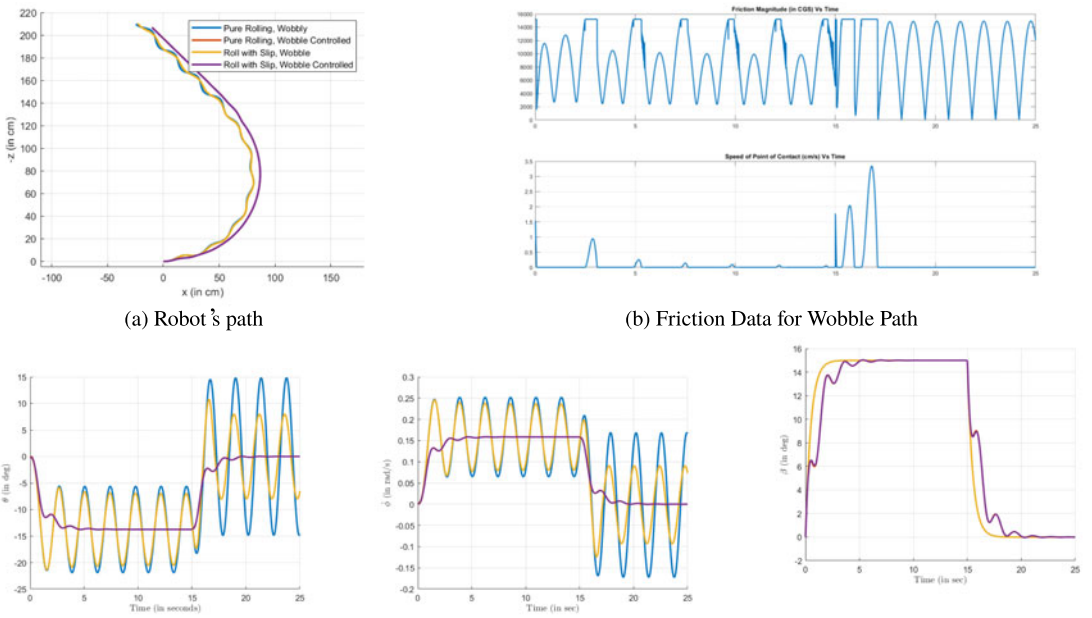
https://doi.org/10.1017/S0263574726103464 Published online by Cambridge University Press



(a) Robot's path (b) Wobbling vs. time

(c) Precession rate vs. time (d) Pendulum Angle vs. time

Figure 10. *Comparison between wobbly and wobble-free motion when $\beta_{des} = 15°$ during turning motion.*



(a) Robot's path (b) Friction Data for Wobble Path

(c) Wobbling vs. time (d) Precession rate vs. time (e) Pendulum Angle vs. time

Figure 11. *Comparison of wobbly and wobble-free motion when $\beta_{des} = 15°$ in low friction regions.*

As depicted in Figure 10c, the linear combination-based controller (T_p) also stabilizes the precession rate. When comparing the initial 15 s of motion, a noticeable contrast in the amplitude of oscillation in the precession rate $\dot{\phi}$ becomes evident between the wobbly motion case (0.0936 rad/s) and the motion without wobble (3.06×10^{-6}). In the period where the robot executes a wobble-free turning motion,

https://doi.org/10.1017/S0263574726103464 Published online by Cambridge University Press

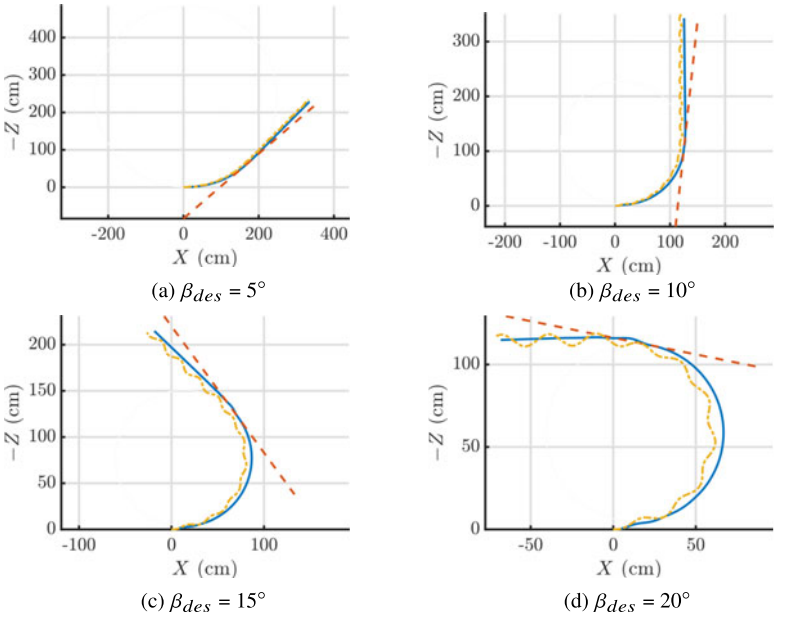


Figure 12. *Comparison between the path taken by the robot during wobbly and wobble-free turning motion while moving with different value of pendulum angle during the circular arc.*

the figure illustrates a precession rate of 0.158 rad/s. Furthermore, when the robot transitions to moving along a straight line, the precession rate reduces to zero.

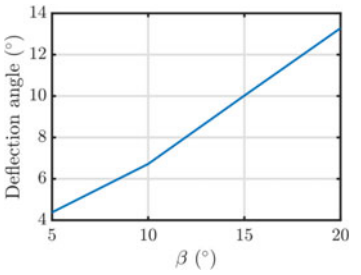
The evolution of the pendulum angle β over time, as depicted in Figure 10d, demonstrates its practical feasibility. Interestingly, the behavior of β during the robot's wobbly motion is characterized by a smooth response that is neither oscillatory nor monotonically increasing or decreasing. However, when the robot transitions into a wobble-free motion facilitated by the linear combination-based controller (T_p), the response of β exhibits transient oscillations. Eventually, it stabilizes at a mean value of 15° with an amplitude of 3.63×10^{-4}. It is important to highlight that the oscillatory behavior observed in β during the wobble-free motion also diminishes as the robot approaches a steady state.

Figure 12 illustrates a comparison between wobbly and wobble-free turning maneuvers with the proposed controller for varying pendulum angle β values at forward speed $\dot{\psi}$ of 1 rad/s. The solid line style represents motion without wobble, whereas the dash-dotted line style represents motion with wobble. During the circular arc section of the path, we can observe that the radius of curvature for these two types of response varies slightly. After the turning maneuver, both trajectories converge to move in the same direction.

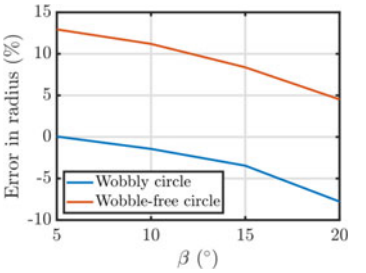
The dotted line style represents the circle that the wobble-free turning maneuver is a part of while tracing the circular arc. The dashed line represents the tangent to this circle at the point where β_{des} is toggled to 0°. Due to the settling time associated with this toggle command, the tangent at the toggle point is not parallel to the direction of the final straight line for both wobbly and wobble-free straight lines. This deflection is shown as a function of pendulum angle β in Figure 13a. Observably, the deflection increases as the angle of the pendulum increases.

At a given speed of operation, the radius of curvature during a turning maneuver can be approximated using the Eq. (41) for various values of pendulum angle β. This approximation holds true as long as the magnitude of β remains below 20°. The error in the radius of curvature is depicted in 13b as the percentage difference between the observed values and the desired values predicted by Eq. (41). For both wobbly and wobble-free motion, the percentage error in the radius of curvature relative to the desired value decreases as the pendulum angle increases. In conclusion, when the inclination of the pendulum is altered, the heading angle deflection and error in the radius of curvature exhibit opposite behaviors.

https://doi.org/10.1017/S0263574726103464 Published online by Cambridge University Press

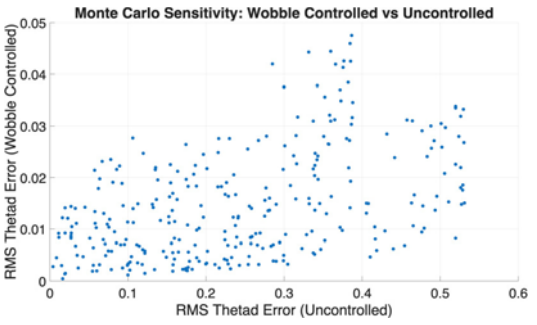


(a) Deviation from the tangent at the end of circular arc in turning motion

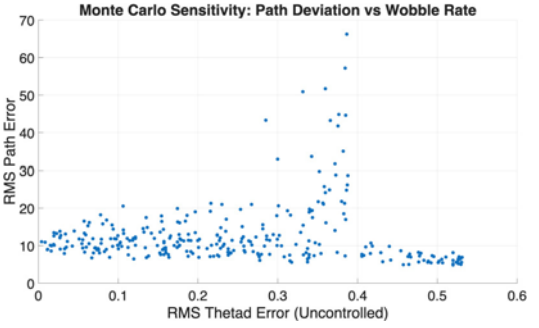


(b) Error in radius of curvature observed in turning motion compared to values obtained from Eqn. (41)

Figure 13. *Errors as a function of β.*



(a) RMS $\dot{\theta}$ Error



(b) RMS Path Error

Figure 14. *Monte Carlo sensitivity analysis on the effect of parametric perturbations on (a) wobble rate and (b) trajectory deviation.*

Based on heading deflection tolerance and acceptable error in the radius of curvature, Figure 13a and b can be used to choose a pendulum angle that corresponds to the desired operational speed.

4.3. Sensitivity analysis

To evaluate the robustness of the proposed controller, a Monte Carlo–based sensitivity analysis was performed by introducing parametric uncertainties in both geometric and inertial properties of the system. Specifically, the parameters R_p, R_s, M_p, M_s, and M_y were randomly perturbed within a range of $\pm 5\%$ around their nominal values ($R_s = 12$ cm, $R_y = 0$ cm, $R_p = 10$ cm, $M_s = 800$ g, $M_p = 200$ g, $M_y = 550$ g). This was iterated over 300 samples, and the following analysis was performed.

For each sampled parameter set, the system response was simulated under both wobble-controlled and uncontrolled conditions. The robustness of the controller was quantified using the root mean square (RMS) error of the wobble rate, $\dot{\theta}$, computed with respect to the nominal trajectory. In addition, the deviation in spatial trajectory was evaluated using the RMS path error in the x–z plane.

The results of the Monte Carlo analysis in Figure 14 demonstrate that the proposed controller consistently reduces the wobble rate across the entire parameter space. This is evident from the distribution of RMS errors, where the controlled cases exhibit significantly lower values compared to their uncontrolled counterparts for the majority of sampled configurations. This indicates that the controller maintains stable performance despite moderate variations in system parameters.

A correlation-based sensitivity analysis was further conducted to quantify the influence of each parameter on system performance, where the Pearson correlation coefficient (computed using `corrcoef`

https://doi.org/10.1017/S0263574726103464 Published online by Cambridge University Press

Table I. *Correlation-based sensitivity of parameters with RMS wobble rate and trajectory deviation.*

Parameter	$\lvert\text{Corr}(\dot{\theta}_{\text{RMS}})\rvert$	$\lvert\text{Corr}(\text{Path Error}_{\text{RMS}})\rvert$
R_p	−0.1294	−0.5356
R_s	0.1264	0.6259
M_p	−0.0484	0.0070
M_s	−0.0026	0.1053
M_y	−0.0761	−0.0941

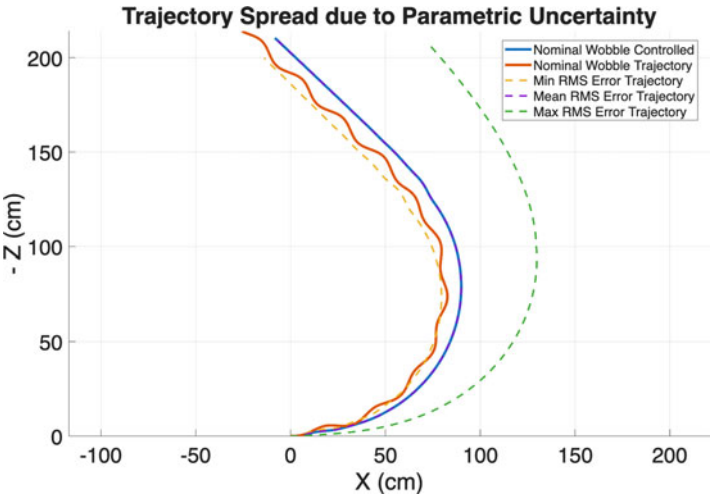


Figure 15. *Trajectory spread due to parametric uncertainty. The nominal wobble-controlled and uncontrolled trajectories are shown along with trajectories corresponding to minimum, mean, and maximum RMS path deviations from the uncontrolled wobbly trajectory.*

in MATLAB) measures the linear dependence between parameter variations and performance metrics. The results reveal that geometric parameters, particularly R_p and R_s, have the most significant impact on path deviation, while inertial parameters contribute comparatively less (Table I). In contrast, the wobble dynamics, quantified through the RMS error of $\dot{\theta}$, are influenced by both geometric and inertial properties, with R_p, R_s, and M_y exhibiting the highest sensitivity.

The trajectory spread illustrated in Figure 15 provides further insight into the effect of parameter uncertainty. The controlled trajectories remain tightly clustered around the nominal path for low and mean path error cases, indicating strong robustness in typical operating conditions. However, the trajectory corresponding to the maximum RMS path error deviates significantly, forming a pronounced outer envelope. Only 5% of the samples show large deviations (path deviation $\approx > 30$ *cm*), indicating that specific configurations tend to make these outliers. This can be seen in the scatter plot in Figure 14b. Most samples fit closely to the nominal path so much so that the trajectory corresponding to the mean RMS error almost coincides with the nominal controlled trajectory. This suggests that while the controller performs reliably for most parameter variations, certain combinations – primarily involving geometric perturbations – can lead to amplified deviations.

This observation is reinforced by Table II, which lists the parameter sets corresponding to the largest path errors. These outliers show consistent shifts in geometric parameters (R_p, R_s) relative to their nominal values, whereas inertial parameters vary without a clear dominant pattern. This confirms that geometric inaccuracies have a more critical impact on trajectory tracking than inertial uncertainties. This suggests that the worst deviations happen when R_p reduces and R_s increases, effectively decreasing the effect of the pendulum in steering the robot.

https://doi.org/10.1017/S0263574726103464 Published online by Cambridge University Press

Table II. *Top 10 parameter samples corresponding to the largest RMS path errors obtained from the Monte Carlo sensitivity analysis.*

R_p	R_s	M_p	M_s	M_y	**RMS** $\dot{\theta}$	**RMS Path Error**
9.5205	12.508	203.07	834.61	531.49	0.3865	66.220
9.5133	12.477	193.93	767.47	539.41	0.3846	57.192
9.6067	12.554	190.09	821.99	567.45	0.3596	51.699
9.5377	12.462	208.27	823.69	527.93	0.3314	50.910
9.6192	12.528	202.91	798.36	557.66	0.3766	44.832
9.6098	12.521	193.75	781.29	566.38	0.3853	44.583
9.6320	12.530	209.12	806.02	525.79	0.2849	43.315
9.6679	12.574	204.25	800.04	548.41	0.3660	43.223
9.6536	12.544	200.82	814.38	524.51	0.3755	41.750
9.6209	12.435	199.69	827.59	534.02	0.3820	35.059

These findings highlight that the proposed control strategy is robust to variations in both geometric and inertial parameters, while also emphasizing that accurate geometric modeling is critical for minimizing trajectory deviations. This analysis demonstrates that the controller is reliable under realistic parametric uncertainties and further validates its applicability to practical implementations.

5. Point-to-point navigation with wobble controller

In order to test the controller in more complex navigation tasks, we implemented a point-to-point navigation algorithm as studied in a previous work from our lab [8]. In this section, we study the efficiency of the wobble controller in navigation for various trajectories that achieve a higher complexity when compared to circular or straight-line motion.

5.1. Approach

For this navigation algorithm, we consider that the robot moves at a constant speed of $|\dot{\psi}| = 1$ rad/s. The steering is governed by adjusting the pendulum angle β based on the angle σ made between the velocity vector $\vec{v}$ and the vector from the robot to the target location $\vec{r}$. The pendulum angle varies smoothly between $+15^\circ$ and -15°, with a sigmoid function used to interpolate between the extremes and eliminate the discontinuity.

The navigation objective is to initially maintain heading until angle $\sigma \in [-\frac{\pi}{2}, \frac{\pi}{2}]$, after which σ is minimized to steer the robot towards the target location as seen in Figure 16. Let σ_{init} be the angle the robot makes with the target at the start of the trajectory, and let t_B be the first time instance where $abs(\sigma) \leq \frac{\pi}{2}$. Then at any time t, the pendulum angle β is computed as follows:

∗∗The method and proof of navigation can be further referred from [8]

Algorithm 1 *Calculate the instantaneous target angle*

1: Calculate the instantaneous target angle σ_t
2: **if** $t \geq t_B$ **then**
3: $\beta = 15^\circ \times (2 \times \text{sigmoid}(K \sin(\sigma_t)) - 1)$ (K: tuning constant for sigmoid function)
4: **else**
5: $\beta = 15^\circ \times (2 \times \text{sigmoid}(K \sin(\sigma_{init})) - 1)$
6: **end if**

https://doi.org/10.1017/S0263574726103464 Published online by Cambridge University Press

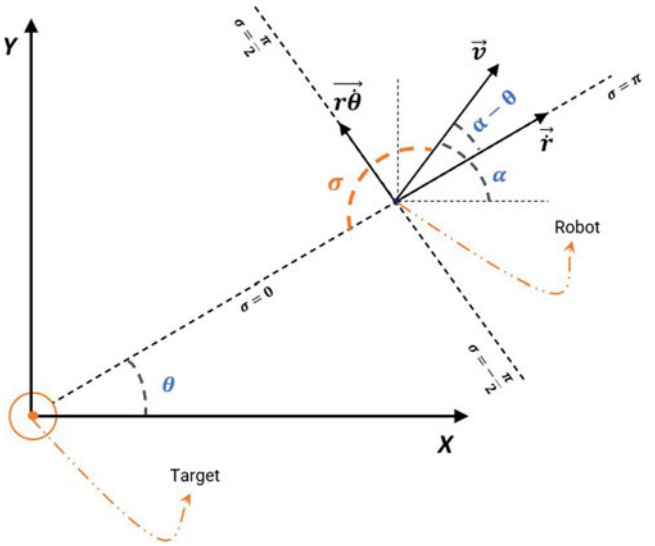
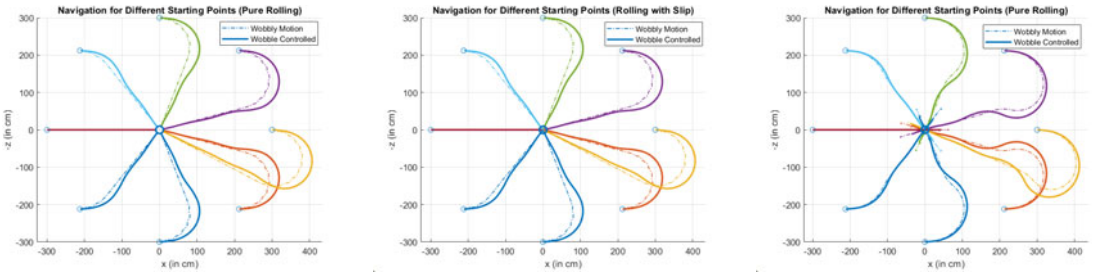


Figure 16. *Illustration of navigation at a time instant.*



(a) Pure Rolling (b) Friction Coeff μ = 0.01 (c) Friction Coeff. μ = 0.0015

Figure 17. *Navigation under various slip conditions.*

5.2. Results

Navigation was simulated under four distinct conditions: (i) pure rolling with wobble control, (ii) pure rolling without wobble control, (iii) rolling with slip with wobble control, and (iv) rolling with slip without wobble control. These simulations were conducted from multiple initial positions located on the circumference of a circle with radius 300, with the target point fixed at the origin. This setup was chosen to evaluate the robustness of the navigation algorithm and, by extension, the wobble controller across a variety of possible scenarios.

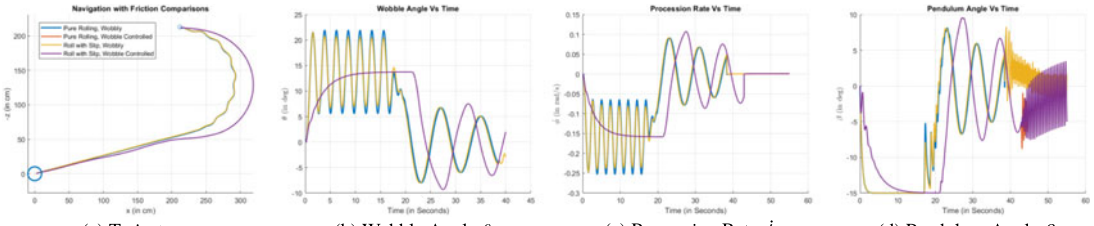
The results for the four conditions are seen in the following plots. Figure 17 has two plots, each comparing wobble-controlled and wobbly motion starting from different points. The coefficient of friction for these is $\mu = 0.01$. We notice here that the system quickly stops slipping and rolling, and the effect of friction is not that prominent. However, as we lower the coefficient of friction to $\mu = 0.0015$, we can see the effect of slipping in Plots 18, 19, and 20. Each graph includes both a controlled and wobbly (uncontrolled) plot for direct comparison.

The RMS error of $\dot{\theta}$ and the path length with and without wobble control are documented in Table III. From the table, we can infer that as the robot begins to slip, the RMS error of $\dot{\theta}$ increases (comparing Table IIIa and IIIc). This means that the system is more susceptible to wobble. We also infer that the path length overall increases. However, the difference between the controlled path length and the uncontrolled path length reduces. This happens because slipping reduces the effect of wobble (θ) on the linear motion of the center.

https://doi.org/10.1017/S0263574726103464 Published online by Cambridge University Press

Table III. *Path lengths and RMS lean rate errors friction coefficients μ of paths taken from Figure 17.*

Start (x,z) [cm]	**Path w/o control [cm]**	**Path w/control [cm]**	**RMS $\dot{\theta}$ error [rad/s]**
(0, 300)	354.1391	384.8390	0.1826
(212, 212)	460.6939	508.8795	0.1940
(300, 0)	577.9033	626.9113	0.1936
(212, −213)	460.6776	508.9161	0.1932
(0, −300)	354.1526	384.8019	0.1833
(− 213, −213)	299.2201	305.2644	0.1414
(− 300, −1)	289.7280	289.7280	0.0000
(− 213, 212)	299.1492	305.2199	0.1433
(a) Pure rolling			
Start (x,z) [cm]	Path w/o control [cm]	Path w/control [cm]	RMS $\dot{\theta}$ error [rad/s]
(0, 300)	362.4208	396.7085	0.1603
(212, 212)	477.2967	522.2828	0.1539
(300, 0)	585.6486	636.5021	0.1638
(212, −213)	477.2522	522.2832	0.1542
(0, −300)	376.5530	392.0286	0.1599
(− 213, −213)	324.3173	317.9721	0.1316
(− 300, −1)	315.8823	311.0216	0.0882
(− 213, 212)	306.4115	325.5624	0.1401
(b) $\mu = 0.01$			
Start (x,z) [cm]	Path w/o control [cm]	Path w/control [cm]	RMS $\dot{\theta}$ error [rad/s]
(0, 300)	453.9082	449.9122	0.4003
(212, 212)	624.0027	593.6773	0.3979
(300, 0)	694.2351	727.6145	0.2449
(212, −213)	624.5491	588.0787	0.4130
(0, −300)	477.1634	449.8817	0.3793
(− 213, −213)	437.6789	355.0896	0.4699
(− 300, −1)	366.7502	346.0108	0.4691
(− 213, 212)	436.3991	355.0309	0.4676
(c) $\mu = 0.0015$			

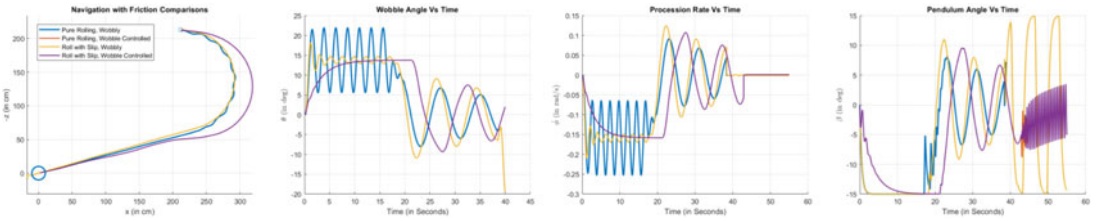


(a) Trajectory (b) Wobble Angle θ (c) Procession Rate $\dot{\phi}$ (d) Pendulum Angle β

Figure 18. *State variables during point-to-point navigation ($\mu = 0.01$).*

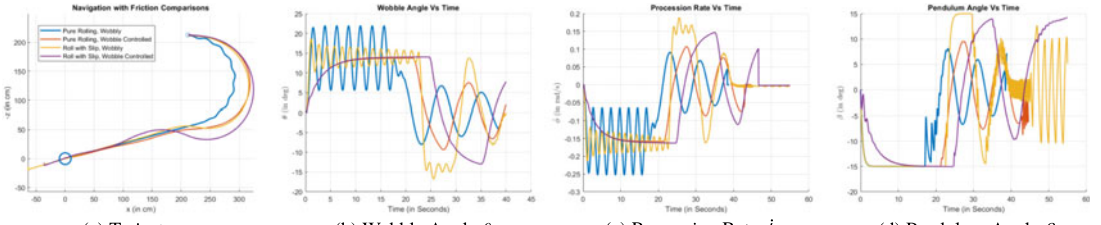
As seen in the plots, the sensitivity of pendulum angle β reduces when the wobble controller is active even with an idealistic controller, and this is particularly highlighted here as the controlled trajectory is offset; however, it still reaches the target. We also see that, despite the low coefficients of friction, the navigation and wobble controller work with high robustness, and the desired goal of mitigating wobble is achieved.

https://doi.org/10.1017/S0263574726103464 Published online by Cambridge University Press



(a) Trajectory (b) Wobble Angle θ (c) Procession Rate $\dot{\phi}$ (d) Pendulum Angle β

Figure 19. *State variables during point-to-point navigation ($\mu = 0.003$).*



(a) Trajectory (b) Wobble Angle θ (c) Procession Rate $\dot{\phi}$ (d) Pendulum Angle β

Figure 20. *State variables during point-to-point navigation ($\mu = 0.0015$).*

6. Conclusion and future work

This article proposes a dynamic model of a pendulum-actuated spherical robot considering the coupling between forward and steering motion. Our model qualitatively captures the system's lateral oscillations, which we refer to as wobbling. Modeling the wobble allows for the investigation of controller design for stabilizing the yoke, which serves as a platform for mounting sensors on a spherical robot. The yoke must remain stable during motion because the sensors mounted on the yoke would otherwise produce inaccurate results. In addition, we present mathematical formulations for the robot's radius of curvature, precession rate, wobble amplitude, and wobble frequency when moving in a wobbly circular motion. We design a controller for the non-holonomic spherical robot using only two input torques. We finally demonstrate the controller's robustness for various motions of pure rolling and slipping conditions using a point-to-point navigation algorithm and documenting the wobble rate and path length. The controller design aims towards controlling the forward speed $\dot{\psi}$, pendulum angle β, and limiting wobble (oscillations in the lean angle θ).

The proposed controller assumes full state sensing. This makes experimental validation quite challenging. Future work will focus on the development of robot hardware as well as experimental techniques to achieve accurate and reliable full-scale sensing. This is an even bigger challenge in the presence of slip. Observer-based methods to estimate some of the states may also be looked into for motions constrained to specific trajectories. Optimization of robot design (intertial parameters and dimensions) and controller parameters can also be explored further.

The results of this work can be applied to the robot's semi-autonomous teleoperation. In this mode, a command is issued for a desired pendulum angle to steer the robot in a specific direction while maintaining a desired forward speed. The wobble controller can assist the robot in moving without wobbling along the desired curve or line even if the robot slips relative to the ground surface.

Author contributions. VB generated the simulations, analyzed, and optimized the mathematical model in depth, created the friction model, and implemented the point-to-point navigation; AS reviewed the relevant prior work, enhanced the mathematical model, designed the controller, and led the writing of the manuscript; SM developed the mathematical model of the robot; AG and LV provided advice and supervision.

Acknowledgements. The authors would like to thank Omkar Ghar for contributing to developing the robot's 3D multibody dynamic simulation in Simulink.

Financial support. This work is funded by a project under NCETIS (National Center of Excellence in Technology and Internal Security), IIT Bombay, sponsored by the Ministry of Electronics and Information Technology.

https://doi.org/10.1017/S0263574726103464 Published online by Cambridge University Press

Competing interests. The authors declare no conflicts of interest exist.

Ethical approval. Not applicable.

References

[1] A. Diouf, B. Belzile, M. Saad and D. St-Onge, "Spherical Rolling Robots - Design, Modeling, and Control: A Systematic Literature Review," **In:** *2024 Robotics and Autonomous Systems*, vol. **175**, (2024) pp. 104657. doi: 10.1016/j.robot.2024.104657.

[2] R. H. Armour and J. F. Vincent, "Rolling in nature and robotics: A review," *J. Bionic Eng.* **3**(4), 195–208 (2006). doi: 10.1016/S1672-6529(07)60003-1.

[3] Q. Zhan, T. Zhou, M. Chen and S. Cai, "Dynamic Trajectory Planning of a Spherical Mobile Robot," **In:** 2006 IEEE Conference on Robotics, Automation and Mechatronics (2006) pp. 1–6. doi: 10.1109/RAMECH.2006.252705.

[4] Q. Zhan, Y. Cai and Z. Liu, "Near-Optimal Trajectory Planning of a Spherical Mobile Robot for Environment Exploration," **In:** 2008 IEEE Conference on Robotics, Automation and Mechatronics (2008) pp. 84–89. doi: 10.1109/RAMECH.2008.4681380.

[5] Y. Mizumura, K. Ishibashi, S. Yamada, A. Takanishi and H. Ishii, "Mechanical Design of a Jumping and Rolling Spherical Robot for Children with Developmental Disorders," **In:** 2017 IEEE International Conference on Robotics and Biomimetics, ROBIO (2017) pp. 1–6. doi: 10.1109/ROBIO.2017.8324558.

[6] N. W. Oumer and T. Ylikorpi, "Development of Wireless Control System for a Spherical Robot," Master's Thesis, Helsinki University of Technology, Espoo, Finland (2009).

[7] A. Singhal, S. S. Modi, A. Gupta, L. Vachhani and O. Ghag, "Pendulum Actuated Spherical Robot: Dynamic Modeling & Analysis for Wobble & Precession," **In:** Proceedings of 22nd IFAC International Symposium on Automatic Control in Aerospace (ACA) vol. **55**(22) (2022) pp. 67–72. doi: 10.1016/j.ifacol.2023.03.012.

[8] V. Dwaracherla, S. Thakar, L. Vachhani, A. Gupta, A. Yadav and S. Modi, "Motion planning for point-to-point navigation of spherical robot using position feedback," *IEEE/ASME Trans. Mechatron.* **24**(5), 2416–2426 (2019). doi: 10.1109/TMECH.2019.2934789.

[9] J. Froberg and M. Smolic, "A Dirigible Bowling Ball: Controlling a Bowling Ball to Hit a Strike Every Time," Bachelor's Thesis, KTH Royal Institute of Technology, Stockholm, Sweden (2021).

[10] G. C. Schroll, "Dynamic Model of a Spherical Robot From First Principles," Master's Thesis, Colorado State University, Fort Collins, CO, USA (2010).

[11] M. A. Arif, A. Zhu, H. Mao and Y. Tu, "Panoramic visual system for spherical mobile robots," *Robotica* **42**(7), 2089–2107 (2024). doi: 10.1017/S0263574724000043.

[12] V. A. Joshi, R. N. Banavar and R. Hippalgaonkar, "Design and analysis of a spherical mobile robot," *Mech. Mach. Theory* **45**(2), 130–136 (2010). doi: 10.1016/j.mechmachtheory.2009.04.003.

[13] V. A. Joshi and R. N. Banavar, "Motion analysis of a spherical mobile robot," *Robotica* **27**(3), 343–353 (2009). doi: 10.1017/S0263574708004748.

[14] M. Roozegar, M. Ayati and M. J. Mahjoob, "Mathematical modelling and control of a nonholonomic spherical robot on a variable-slope inclined plane using terminal sliding mode control," *Nonlinear Dyn.* **90**(2), 971–981 (2017). doi: 10.1007/s11071-017-3705-9.

[15] R. Lin, T. Li, J. Huo and Q. Wang, "Research on motion control of spherical robot in slope environment," *Robotica* **43**(5), 1910–1928 (2025). doi: 10.1017/S0263574725000591.

[16] S. B. Chen, A. Beigi, A. Yousefpour, F. Rajaee, H. Jahanshahi, S. Bekiros, R. A. Martinez and Y. Chu, "Recurrent neural network-based robust nonsingular sliding mode control with input saturation for a non-holonomic spherical robot," *IEEE Access* **8**, 188441–188453 (2020). doi: 10.1109/ACCESS.2020.3030775.

[17] K. Schröder, G. Garcia, R. Chacón, G. Montenegro, A. Marroquín, G. Farias, S. Dormido-Canto and E. Fabregas, "Development and control of a real spherical robot," *Sensors (Basel)* **23**(8), 3895 (2023). doi: 10.3390/s23083895.

[18] Y. Cai, Q. Zhan and C. Yan, "Two-state trajectory tracking control of a spherical robot using neurodynamics," *Robotica* **30**(2), 195–203 (2012). doi: 10.1017/S0263574711000518.

[19] H. Mao, A. Zhu, X. Wang, M. Li, Y. Zhang, D. Zhang, C. Li, C. Zheng, P. Ma, X. Wu and J. Zhang, "Adaptive high-speed sliding mode control for enhanced maneuverability and trajectory tracking in spherical robots: Adaptive high-speed sliding mode control for enhanced maneuverability," *Nonlinear Dyn.* **114**(4), 231 (2026). doi: 10.1007/s11071-025-12083-2.

[20] Y. Liu, Y. Wang, X. Guan, T. Hu, Z. Zhang, S. Jin, Y. Wang, J. Hao and G. Li, "Direction and trajectory tracking control for nonholonomic spherical robot by combining sliding mode controller and model prediction controller," *IEEE Robot. Autom. Lett.* **7**(4), 11617–11624 (2022). doi: 10.1109/LRA.2022.3203224.

[21] F. R. Hogan and J. R. Forbes, "Trajectory tracking, estimation, and control of a pendulum-driven spherical robot," *J. Guid. Control Dyn.* **39**(5), 1119–1125 (2015). doi: 10.2514/1.G001458.

[22] J. Culebro, J. L. Aguirre and S. Munoz, "Lagrangian Model, Simulation and Control of a Spherical Robot," **In:** 2013 10th International Conference on Electrical Engineering, Computing Science and Automatic Control (CCE) (2013) pp. 1–6. doi: 10.1109/ICEEE.2013.6676019.

[23] D. Liu, H. Sun and Q. Jia, "Stabilization and Path Following of a Spherical Robot," **In:** 2008 IEEE Conference on Robotics, Automation and Mechatronics (2008) pp. 676–682. doi: 10.1109/RAMECH.2008.4681358.

[24] D. Liu, H. Sun, Q. Jia and L. Wang, "Motion Control of a Spherical Mobile Robot by Feedback Linearization," **In:** 2008 7th World Congress on Intelligent Control and Automation (2008) pp. 965–970. doi: 10.1109/WCICA.2008.4593051.

https://doi.org/10.1017/S0263574726103464 Published online by Cambridge University Press

[25] M. Kamaldar, M. J. Mahjoob, M. H. Yazdi, H. Vahid-Alizadeh and S. Ahmadizadeh, "A Control Synthesis for Reducing Lateral Oscillations of a Spherical Robot," **In:** 2011 IEEE International Conference on Mechatronics (2011) pp. 546–551. doi: 10.1109/ICMECH.2011.5971346.
[26] V. A. Crossley, *A Literature Review On the Design of Spherical Rolling Robots* (Carnegie Mellon University, Pittsburgh, PA, 2006) pp. 1–6. Preprint.
[27] R. Chase and A. Pandya, "A review of active mechanical driving principles of spherical robots," *Robotics* **1**(1), 3–23 (2012). MDPI.
[28] A. Halme, T. Schonberg and Y. Wang, "Motion Control of a Spherical Mobile Robot," **In:** Proceedings of 4th IEEE International Workshop on Advanced Motion Control - AMC '96 - MIE, vol. **1** (1996) pp. 259–264. doi: 10.1109/AMC.1996.509415.
[29] S. Mahboubi, M. M. S. Fakhrabadi and A. Ghanbari, "Design and implementation of a novel spherical mobile robot," *J. Intell. Robot. Syst.* **71**(1), 43–64 (2013). doi: 10.1007/s10846-012-9748-8.
[30] F. Michaud and S. Caron, "Roball, the rolling robot," *Auton. Robot.* **12**(2), 211–222 (2002). doi: 10.1023/A:1014005728519.
[31] J. -C. Yoon, S. -S. Ahn and Y. -J. Lee, "Spherical Robot with New Type of Two-Pendulum Driving Mechanism," **In:** 2011 15th IEEE International Conference on Intelligent Engineering Systems (2011) pp. 275–279. doi: 10.1109/INES.2011.5954758.
[32] D. V. Balandin, M. A. Komarov and G. V. Osipov, "A motion control for a spherical robot with pendulum drive," *J. Comput. Syst. Sci. Int.* **52**(4), 650–663 (2013). doi: 10.1134/S1064230713040047.
[33] H. Mao, A. Zhu, Y. Tu, Z. Zhang, D. Li, Y. Zhang and Z. Guo, "A Spherical Mobile Robot Driven by Eccentric Pendulum and Self-stabilizing by Flywheel," **In:** Proceedings of the 2020 17th International Conference on Ubiquitous Robots (UR) (2020). pp. 169–174. doi: 10.1109/UR49135.2020.9144903.
[34] Z. Sheng, F. Xiang, Z. Shouqiang and D. Kai, "Kinetic model for a spherical rolling robot with soft shell in a beeline motion," *J. Multimed.* **9**(2) (2014). 223–229. doi: 10.4304/jmm.9.2.223-229.
[35] S. Asiri, F. Khademianzadeh, A. Monadjemi and P. Moallem, "The design and development of a dynamic model of a low-power consumption, two-pendulum spherical robot," *IEEE/ASME Trans. Mechatron.* **24**(5), 2406–2415 (2019). doi: 10.1109/TMECH.2019.2934180.
[36] B. Belzile and D. St-Onge, "Design and Modeling of a Spherical Robot Actuated by a Cylindrical Drive," **In:** 2022 International Conference on Robotics and Automation (ICRA) (2022) pp. 1169–1175. doi: 10.1109/ICRA46639.2022.9812148.
[37] A. Rosen, "Modified lagrange method to analyze problems of sliding and rolling," *J. Appl. Mech.* **67**(4), 697–704 (2000). doi: 10.1115/1.1328088.
[38] A. M. Bloch, *Nonholonomic Mechanics and Control* (Springer, New York, USA, 2003).
[39] L. Linsong and Q. Zhan, "Dynamic model based on Boltzmann-Hamel equation and adaptive sliding mode trajectory tracking control of spherical mobile robot," *J. ACM* **192**(C), (2025) pp. 105048. doi: 10.1016/j.robot.2025.105048.
[40] T. Ylikorpi, P. Forsman, A. Halme and J. Saarinen, "Unified Representation of Decoupled Dynamic Models for Pendulum-driven Ball-shaped Robots," **In:** Proceedings of the 28th European Conference on Modelling and Simulation (2014). doi: 10.7148/2014-0411.
[41] D. Liu, H. Sun and Q. Jia, "A Family of Spherical Mobile Robot: Driving Ahead Motion Control by Feedback Linearization," **In:** 2008 2nd International Symposium on Systems and Control in Aerospace and Astronautics (2008) pp. 1–6. doi: 10.1109/ISSCAA.2008.4776275.
[42] T. Ylikorpi, P. Forsman and A. Halme, "Gyroscopic Precession in Motion Modelling of Ball-Shaped Robots," **In:** Proceedings of the 28th European conference on modelling and simulation, ECMS (2014) (2014) pp. 401–410. doi: 10.7148/2014-0401.
[43] E. Kayacan, Z. Y. Bayraktaroglu and W. Saeys, "Modeling and control of a spherical rolling robot: A decoupled dynamics approach," *Robotica* **30**(4), 671–680 (2012). doi: 10.1017/S0263574711000956.
[44] M. Nagai, "Control System for a Spherical Robot," Master's Thesis, Luleå University of Technology, Luleå, Sweden (2008).
[45] Y. Cai, Q. Zhan and X. Xi, "Path tracking control of a spherical mobile robot," *Mech. Mach. Theory* **51**, 58–73 (2012). doi: 10.1016/j.mechmachtheory.2011.12.009.
[46] S. Bhattacharya and S. K. Agrawal, "Spherical rolling robot: A design and motion planning studies," *IEEE Trans. Robot. Autom.* **16**(6), 835–839 (2000). doi: 10.1109/70.897794.
[47] S. Bhattacharya and S. K. Agrawal, "Design, Experiments and Motion Planning of a Spherical Rolling Robot," **In:** Proceedings of the IEEE International Conference on Robotics and Automation, vol. **2** (2000) pp. 1207–1212. doi: 10.1109/ROBOT.2000.844763.

A. Appendix

A.1. Lagrange d'Alembert expansion

$\mathbf{M}(q)$ is the 6×6 Inertia matrix with elements: (Note: all elements not mentioned $M_{i,j} = 0$)

$$M_{1,2} = 1, \qquad M_{2,1} = 1,$$
$$M_{1,4} = -r_h \cos\phi, \qquad M_{1,5} = -r_h \cos\theta \sin\phi,$$
$$M_{2,4} = -r_h \sin\phi, \qquad M_{2,5} = r_h \cos\theta \cos\phi,$$
$$M_{3,1} = -m_p r_p \sin(\theta + \beta)\cos\phi, \qquad M_{3,2} = m_p r_p \sin(\theta + \beta)\sin\phi,$$

https://doi.org/10.1017/S0263574726103464 Published online by Cambridge University Press

$$
\begin{aligned}
M_{3,3} &= 4I_p \sin^2(\theta+\beta) + I_h + I_y(1+\cos^2\theta), & M_{3,5} &= -\sin\theta\, I_h,\\
M_{4,1} &= -m_p r_p \cos(\theta+\beta)\sin\phi + (m_h+m_y+m_p) r_h \sin\phi, & &\\
M_{4,1} &= -m_p r_p \cos(\theta+\beta)\sin\phi + (m_h+m_y+m_p) r_h \sin\phi, & &\\
M_{4,2} &= -m_p r_p \cos(\theta+\beta)\cos\phi + (m_h+m_y+m_p) r_h \cos\phi, & &\\
M_{4,4} &= I_h + I_y + 4I_p - m_p r_p r_h \cos(\theta+\beta), & M_{4,6} &= 4I_p - m_p r_p r_h \cos(\theta+\beta),\\
M_{5,1} &= -(m_h+m_y+m_p) r_h \cos\theta\cos\phi, & M_{5,2} &= (m_h+m_y+m_p) r_h \cos\theta\sin\phi,\\
M_{5,3} &= -\sin\theta\, I_p + m_p r_p r_h \sin(\theta+\beta)\cos\theta, & M_{5,5} &= I_h,\\
M_{6,1} &= -m_p r_p \cos(\theta+\beta)\sin\phi, & M_{6,2} &= -m_p r_p \cos(\theta+\beta)\cos\phi,\\
M_{6,4} &= 4I_p, & M_{6,6} &= 4I_p,
\end{aligned}
\tag{54}
$$

$\mathbf{C}(q,\dot{q})$ is the 6×6 Coriolis matrix with elements: (Note: all elements not mentioned $C_{i,j}=0$)

$$
\begin{aligned}
C_{1,4} &= -\dot{\phi}\,[-r_h \sin\phi]\,,\\
C_{1,5} &= -\dot{\phi}\,[r_h\cos\theta\cos\phi] + \dot{\theta}\,[r_h\sin\theta\sin\phi]\,,\\
C_{2,4} &= -\dot{\phi}\,[r_h\cos\phi]\,,\\
C_{2,5} &= -\dot{\phi}\,[r_h\cos\theta\sin\phi] - \dot{\theta}\,[r_h\sin\theta\cos\phi]\,,\\
C_{3,4} &= -\dot{\phi}\left[I_y\sin(2\theta) - 4I_p\sin(2\theta+2\beta)\right],\\
C_{3,5} &= -\dot{\theta}\,[I_h\cos\theta]\,,\\
C_{3,6} &= -\dot{\phi}\left[-4I_p\sin(2\theta+2\beta)\right],\\
C_{4,3} &= -\dot{\phi}\left[-I_y\sin\theta\cos\theta + 2I_p\sin(2\theta+2\beta) - m_p r_p r_h\sin(\theta+\beta)\right],\\
C_{4,4} &= -(\dot{\theta}+\dot{\beta})\left[-m_p r_p r_h\sin(\theta+\beta)\right],\\
C_{4,5} &= -\dot{\phi}\,[-I_h\cos\theta]\,,\\
C_{4,6} &= -(\dot{\theta}+\dot{\beta})\left[-m_p r_p r_h\sin(\theta+\beta)\right],\\
C_{5,4} &= -\dot{\phi}\left[\cos\theta\, I_h - m_p r_p r_h\cos(\theta+\beta)\cos\theta\right],\\
C_{5,6} &= -\dot{\phi}\left[-2m_p r_p r_h\cos(\theta+\beta)\cos\theta\right],\\
C_{6,3} &= -\dot{\phi}\left[2I_p\sin(2\theta+2\beta)\right],
\end{aligned}
\tag{55}
$$

$$
\mathbf{g}(q) = g\, m_p r_p \sin(\theta+\beta)\left[0\;0\;0\;1\;0\;1\right]^T, \quad \boldsymbol{\tau} = \left[0\;0\;0\;0\;T_s\;T_p\right]^T, \tag{56}
$$

A.2. Lagrange d'Alembert row operations

Using elementary operations on $\mathbf{R}_3$, $\mathbf{R}_4$, $\mathbf{R}_5$ and $\mathbf{R}_6$ on Eq. (25)

$$
\begin{aligned}
\mathbf{R}_6 &\to \mathbf{R}_6 + \left(m_p r_p\cos(\theta+\beta)\right)(\sin\phi\,\mathbf{R}_2 + \cos\phi\,\mathbf{R}_1)\,,\\
\mathbf{R}_4 &\to \mathbf{R}_4 - \left(-m_p r_p\cos(\theta+\beta) + (m_h+m_y+m_p) r_h\right)(\sin\phi\,\mathbf{R}_2 + \cos\phi\,\mathbf{R}_1)\,,\\
\mathbf{R}_5 &\to \mathbf{R}_5 + \left((m_h+m_y+m_p) r_h\cos\theta\right)(\cos\phi\,\mathbf{R}_2 - \sin\phi\,\mathbf{R}_1)\,,\\
\mathbf{R}_3 &\to \mathbf{R}_3 + \left(m_p r_p\sin(\theta+\beta)\right)(\cos\phi\,\mathbf{R}_2 - \sin\phi\,\mathbf{R}_1)\,.
\end{aligned}
\tag{57}
$$

Cite this article: V. Balaji, A. Singhal, S. Modi, A. Gupta and L. Vachhani (2026). "Wobble control of a pendulum-based spherical robot", Robotica **44**, 1325–1355. https://doi.org/10.1017/S0263574726103464

https://doi.org/10.1017/S0263574726103464 Published online by Cambridge University Press